



HAL
open science

Geophysical characterisation of active thermogenic oil seeps in the salt province of the lower Congo basin. Part II: A regional validation

Romain Jatiault, Lies Loncke, Damien Dhont, Dominique Dubucq, Patrice Imbert

► To cite this version:

Romain Jatiault, Lies Loncke, Damien Dhont, Dominique Dubucq, Patrice Imbert. Geophysical characterisation of active thermogenic oil seeps in the salt province of the lower Congo basin. Part II: A regional validation. *Marine and Petroleum Geology*, 2019, 103, pp.773 - 791. 10.1016/j.marpetgeo.2019.02.002 . hal-04501008

HAL Id: hal-04501008

<https://hal.science/hal-04501008>

Submitted on 12 Mar 2024

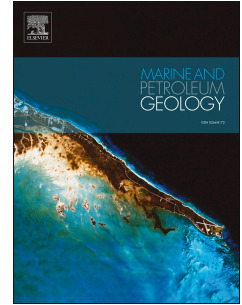
HAL is a multi-disciplinary open access archive for the deposit and dissemination of scientific research documents, whether they are published or not. The documents may come from teaching and research institutions in France or abroad, or from public or private research centers.

L'archive ouverte pluridisciplinaire **HAL**, est destinée au dépôt et à la diffusion de documents scientifiques de niveau recherche, publiés ou non, émanant des établissements d'enseignement et de recherche français ou étrangers, des laboratoires publics ou privés.

Accepted Manuscript

Geophysical characterisation of active thermogenic oil seeps in the salt province of the lower Congo basin. Part II: A regional validation

Romain Jatiault, Lies Loncke, Damien Dhont, Dominique Dubucq, Patrice Imbert



PII: S0264-8172(19)30056-X

DOI: <https://doi.org/10.1016/j.marpetgeo.2019.02.002>

Reference: JMPG 3715

To appear in: *Marine and Petroleum Geology*

Received Date: 25 September 2018

Revised Date: 30 January 2019

Accepted Date: 1 February 2019

Please cite this article as: Jatiault, R., Loncke, L., Dhont, D., Dubucq, D., Imbert, P., Geophysical characterisation of active thermogenic oil seeps in the salt province of the lower Congo basin. Part II: A regional validation, *Marine and Petroleum Geology* (2019), doi: <https://doi.org/10.1016/j.marpetgeo.2019.02.002>.

This is a PDF file of an unedited manuscript that has been accepted for publication. As a service to our customers we are providing this early version of the manuscript. The manuscript will undergo copyediting, typesetting, and review of the resulting proof before it is published in its final form. Please note that during the production process errors may be discovered which could affect the content, and all legal disclaimers that apply to the journal pertain.

1 **Geophysical characterisation of active thermogenic oil seeps in the** 2 **salt province of the Lower Congo Basin. Part II: A regional validation**

3 Romain Jatiault ^{a, b*}, Lies Loncke ^b, Damien Dhont ^a, Dominique Dubucq ^a, Patrice Imbert ^a

4 ^a Total SA, Centre Scientifique et Technique Jean Feger (CSTJF), Avenue Larribau, 64018 Pau, France

5 ^b University of Perpignan Via Domitia, Centre de Formation et de Recherche sur les Environnements Méditerranéens (CEFREM), UMR 5110, 52 Avenue Paul
6 Alduy, 66100 Perpignan, France

7 **Key words:** *Oil slicks, Thermogenic fluid seeps, Pockmarks, Asphalt, Salt diapir, Lower Congo Basin,*
8 *Gas hydrates, Double BSR*

9 ***Abstract***

10 The Lower Congo Basin is known to discharge a substantial volume of oil towards the sea surface,
11 from more than one hundred seafloor seep sites distributed throughout the deep province of the
12 Lower Congo Basin. A large geochemical coring survey confirmed the presence of oil on the seabed.
13 The combination with the seismic data considerably improved the identification of the origin of the
14 oil slicks on the seabed. Multiple specific geophysical characteristics of thermogenic hydrocarbon
15 seep sites were highlighted in a previous detailed analysis of seismic datasets. This study aims to test
16 the characteristics previously identified at regional-scale. The active discharge zone is limited to the
17 distal province of the basin. It is characterized by strong compression / shortening due to the sliding
18 of the post-salt super-sequence, resulting in numerous salt diapirs that control the location of
19 seafloor oil seep sites. The paper describes the bathymetric, reflectivity, amplitude and sub-bottom
20 profiler characteristics of a group of thermogenic seep sites. They correspond essentially to
21 submarine mounds or pockmarks of complex and irregular shape surrounded by hummocky mounds.
22 Active oil pockmarks are systematically associated with positive amplitude anomalies on the seabed
23 and are linked to vertical high-amplitude columns rooted in the seismic reflector and associated with
24 the base of the gas hydrate stability zone. The sub-bottom profiler data shows that the hummocky

25 mounds are connected by a network of faults to high-amplitude bodies buried under a consistent
26 sediment thickness. Based on the definition of specific geophysical features (seafloor mounds,
27 complex shape and irregular pockmarks, positive anomalies of seafloor amplitude, high-amplitude
28 vertical pipes), we identified a series of potential oil seep sites at basin scale. The mounds are
29 particularly recognizable using the seismic curvature attribute; we have identified 2946 individual
30 hummocks that are grouped in 50 zones with a density of 35 to 240 per km². They are believed to be
31 associated with asphalt storage on the seafloor and related to the biodegradation of heavy oils
32 during hydrocarbon dysmigration through the sedimentary pile. Unusual double BSRs occur over the
33 study area; these are also a specific feature of thermogenic seep sites. Barely half of the potential
34 sites identified on the seismic datasets are associated with recurrent oil slicks at the sea surface. The
35 proportion of remaining anomalies may be associated with inactive seep sites over the period of
36 satellite-based monitoring or gas-dominated seep sites.

37 **1. Introduction**

38 Characterizing the natural transfer of hydrocarbons from petroleum reservoirs to the seafloor has
39 strong implications on the understanding of the evolution of sedimentary basins (*Gay et al., 2006a*;
40 *Cartwright et al., 2007; Andresen et al., 2011, Anka et al., 2013; Marcano et al., 2013; Serié et al.,*
41 *2017*), deep marine ecosystems inventories (*Charlou et al., 2004; Ondreas et al., 2005; Jones et al.,*
42 *2014*) or submarine geohazards (*Bünz et al., 2005; Hill et al., 2011*), see the review by *Anka et al.*
43 *(2012)*. Pockmarks are among the most common expression of focused fluid flow at the seafloor
44 (*King and MacLean, 1970; Hovland and Judd, 1988; Judd and Hovland, 2007*). Their size and
45 geometry depend on sediment host properties and hydrocarbon flux (*Hovland et al., 2012*). The
46 ascent of fluids through the sedimentary series causes vertical successions of acoustic anomalies on
47 seismic sections (*Cunningham and Lindholm, 2000; Heggland, 2002; Gay et al., 2006b*). They are
48 called either pipes, defined as vertical successions of increasing reflection amplitudes (typically
49 narrow, i.e. up to a few 100m diameter) and known to commonly form large clusters, or chimneys,

50 defined as large-scale (typically > 1 km diameter) and solitary features without any particular internal
51 reflection (*Løseth et al., 2001; Loncke et al., 2004; Cartwright et al., 2007; Løseth et al., 2009;*
52 *Hustoft et al., 2009; Moss and Cartwright, 2010; Løseth et al., 2011; Ho et al., 2012; Karstens et al.,*
53 *2015*). In the case of abundant gas migration towards the seabed, hydrates precipitate at the
54 interface between free gas and hydrate domains. This forms a seismic reflector with a polarity
55 opposite to that of the seabed, known as the Bottom Simulating Reflection (BSR) (*Shipley, 1979;*
56 *Hovland et al., 1997; MacKay et al., 1994; Berndt et al., 2004; Haacke et al., 2007*). The
57 identification of sea surface oil seepage slicks is used throughout the petroleum exploration
58 workflow to validate source rock maturation, from targeting (*Kornacki et al., 1994; Thrasher et al.,*
59 *1996; Williams and Lawrence, 2002; O'Brien et al., 2005; Stalvies et al., 2017*) to prospect validation
60 (*Jauer and Budkewitsch, 2010*). Positioning the outlines of multi-temporal slicks on the same map
61 commonly shows radiating features from the central source area (*De Beukelaer et al., 2003; Jatiault*
62 *et al., 2017*). The spatial imagery was able to detect 50% of potential oil-supplying seep sites
63 identified on exploration seismic in the Gulf of Mexico (*Garcia-Pineda et al., 2010*).

64 Recently, *Serié et al. (2017)* set out a methodology to study hydrocarbon fluid flow by combining
65 remote sensing, seafloor coring campaign and industrial seismic data. The present study relies on this
66 pre-existing methodology that we complemented with a denser dataset of sea surface natural slicks
67 together with high resolution sub-seafloor data. More recently, *Jatiault et al. (2019, Part I)*
68 presented seafloor and sub-seafloor high-resolution characteristics of one active oil seep in the
69 Lower Congo Basin (see details in section 2.2). This complementary study aims at testing the
70 recognition criteria defined for a single oil seep on a larger seep population recognised in the Lower
71 Congo Basin. The combination of sea-surface slicks database, geochemical cores and geophysical
72 anomalies (high-resolution surveys used for geo-hazards evaluation and exploration 3D seismic)
73 made it possible to inventory oil-seep sites over a 35*50 km wide area. The comparison of oil-
74 supplying seeps with the whole set of fluid-flow features at the seafloor and in the shallow
75 subsurface will be used to better discriminate and define seismic features that can potentially be

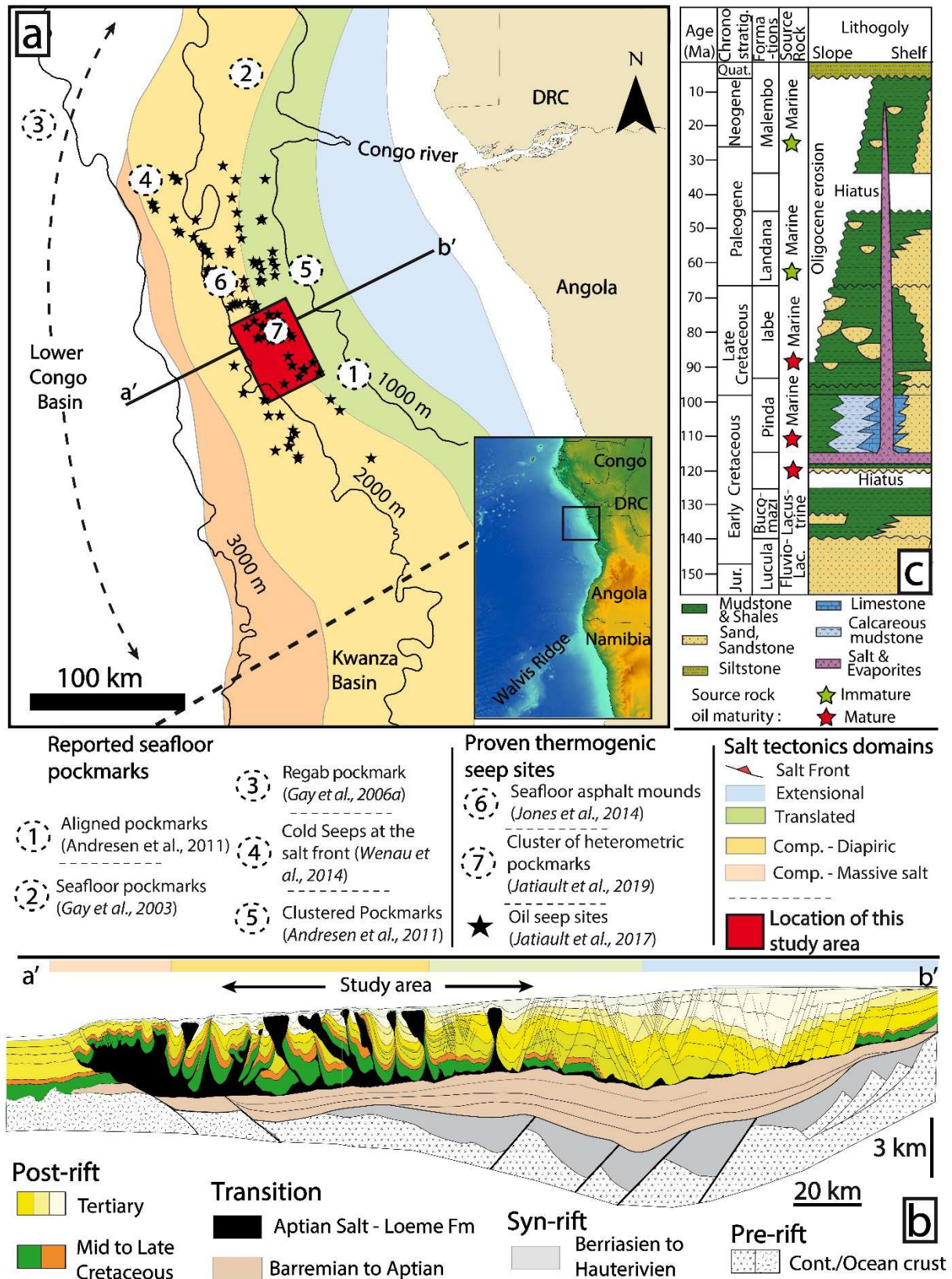
76 diagnostic of oil seep sites. This study discusses about the significance of fluid-related seismic
77 features with an updated methodology integrating for the first time sea surface slicks and
78 geophysical data in the Lower Congo Basin. Active oil seep sites will be compared with potential seep
79 sites identified from geophysical attributes in the Lower Congo Basin.

80 **2. The Lower Congo Basin**

81 **2.1. Geological setting and petroleum systems**

82 The study area located between 10 to 12 °E and 6 to 8°S corresponds to a large oil-seeping province
83 in deep offshore Angola characterised by water depths ranging from roughly 1000 to 3000 m. The
84 chrono-stratigraphic framework of the LCB is divided into 3 major phases after the South Atlantic
85 opening during the Early Cretaceous (144 - 140 Ma). The pre-salt (Berriasian to Barremian)
86 succession consists of extensive lacustrine deposits including the oil-prone (mix type I/II kerogens)
87 **Bucomazi Fm** (Fig. 1c; *Burwood, 1999; MacHargue, 1990; Schoellkopf and Patterson, 2000;*
88 *Brownfield and Charpentier, 2006*). The transitional phase (Late Barremian to Aptian) marks the end
89 of the crustal extension followed by a period of thermal subsidence (*Brice et al., 1982; MacHargue,*
90 *1990; Fort et al., 2004*). The confined environment of the margin together with a drop in the main
91 sea level enabled the deposition of a thick evaporite layer (1000 m thick in average; *Marton et al.,*
92 *2000*; Fig. 1b). The post-salt super-sequence is subdivided into three main episodes. The aggrading
93 stage started with the development of a carbonate-ramp (**Pinda Fm**; 113 - 95 Ma) under stable
94 climatic and restricted marine conditions (*Haq et al., 1987; Séranne, 1999; Séranne and Anka, 2005*).
95 This period continued with a progressive deepening of the basin due to thermal subsidence, leading
96 to the deposition of the oil-prone **Iabe Fm** (99 - 65 Ma, ~10 % TOC; *Burwood, 1999; Cole, 2000*) and
97 subsequent (~4% TOC) **Landana Fm** (65 - 45 Ma; *Cole et al., 2000, Schoellkopf and Patterson, 2000;*
98 Fig. 1c). The pre-salt series are the most prolific source intervals in the basin as Tertiary source rocks
99 are immature over most of it. The Eocene/Oligocene transition corresponds to a period of amplified
100 sea level variations ("Ice house" period; *Séranne, 1999*). It is marked by a regional unconformity,

101 corresponding to a 10 Ma hiatus controversially interpreted as originating from the African
102 superswell (*Nyblade and Robinson, 1994*) or climate fluctuations. The 500 m thick eroded series
103 were transported towards the basin (*Teisserenc and Villemin, 1989; Séranne et al., 1992; Anka et*
104 *al., 2009*). The prograding stage (35 - 5 Ma) corresponds to the establishment of the paleo-Congo
105 during the early Oligocene. It was coupled with an "ice house" period, resulting in the deposition of
106 siliciclastic sediments (**Malembo Fm**). The Miocene-Pliocene transition is marked by the shift of the
107 Congo River to its present-day location. The development of an important upwelling system during
108 the Early Quaternary (*Uenzelmann-Neben, 1998*) resulted in fining-upward sedimentation, leading to
109 fine-grained deposits in the deep sea fan. The post-salt super-sequence is affected by gravitational
110 deformation, sliding over the Aptian salt décollement layer. Salt tectonics subdivided the basin into
111 an upslope extensional domain, a translated area and a downslope compressive province
112 characterised by salt diapirs, which confined the sedimentation to minibasins (*Oluboyo et al., 2014*).



113

114 **Fig. 1: a. Location map of the study area showing the main geological provinces of the LCB. The**115 **map integrates the seafloor seeps reported in the literature (compiled from Gay et al., 2003; Gay**

116 *et al., 2006a; Gay et al., 2007; Andresen et al., 2011; Wenau et al., 2014; Jones et al., 2014*) and
117 recurrent oil slicks at the sea surface (black stars, from *Jatiaux et al., 2017*). Continuous black lines
118 represent 1000 m isobaths (Gebco). b. Regional cross section across the LCB displaying the pre-rift,
119 syn-rift and post-rift sequences (modified from *Jatiaux et al., 2017*). c. Chronostratigraphic log and
120 petroleum system plays (modified from *Anka et al., 2013*).

121 2.2. Literature review of natural hydrocarbon seeps

122 The LCB is affected by a large active fluid seepage system, as revealed during intensive petroleum
123 exploration over the last decade. Seabed outcrops of Miocene series, characterised by extensive high
124 amplitudes above the crest of the salt diapirs, correspond to preferential stratigraphic pathways for
125 migrating fluid in the salt provinces (*Serié et al., 2017*). In the salt minibasins, widespread classical
126 type I pockmarks (Conical; see definition of Type I in *Riboulot et al., 2016*) related to sediment pore
127 dewatering and biogenic methane venting are associated with the polygonal fault networks
128 (*Cartwright 2007; Andresen et al., 2011*). Aligned type I pockmarks commonly follow the maximal
129 flexural syncline axis of the minibasins (No. 1 in Fig. 1a; *Andresen et al., 2011*) or occur as sinuous
130 trends marking the ancient pathways of the Congo canyon (No. 2; *Gay et al., 2003*). A biogenic origin
131 is also suspected for the giant (~2000m diameter) Regab pockmark, located in the deep abyssal plain
132 at a water depth of 3150m (No. 3; *Gay et al., 2006a*). The origin of the gas expelled at the salt front
133 remains undetermined (No. 4; *Wenau et al., 2014*). A thermogenic contribution is highly suspected
134 for isolated pockmarks linked with Miocene turbidite channels (No. 2; *Gay et al., 2006 b*) and for
135 clustered pockmarks linked with salt diapirs (No. 5; *Andresen, 2012*). The migration of thermogenic
136 hydrocarbon is proven from the identification of a large number of seafloor asphalt mounds that
137 spread on top of salt diapirs (n°6; *Jones et al., 2014*). Seafloor asphalt mounds may reach
138 approximately 1m in height and host an abundance of biofauna. From the analysis of spaceborne SAR
139 imagery, *Jatiaux et al. (2017)* calculated that the 100 oil seep sites of the compressive salt domain
140 (black stars in Fig. 1a) emit a volume of $4.38 \cdot 10^6$ litres of oil per year

141 The vertical association of sea-surface slicks and seafloor data show that seafloor seeps correspond
142 to clusters of pockmarks and seafloor mounds (n°7; *Jatiaux et al., 2019, Part I*). One pockmark
143 cluster investigated in detail in *Jatiaux et al., 2019, part I* consists of a complex of heterometric
144 depressions associated with asphalt mounds with diameters of 10 to 15 m in on the seafloor
145 (*Unterseh et al., 2013; Jones et al., 2014*). The subsurface is affected by several geophysical features
146 including a shallow High Impedance Layer (HIL) that reaches the seafloor at the location of
147 depressions on the sub-bottom profiler data. The HIL is interpreted as related to carbonate
148 concretions with a possible contribution of asphalt layers (*Hill et al., 2011*), (2) a set of two parallel
149 reflections, about 50 ms apart, whose polarity is opposite that of the seafloor. They are interpreted
150 as a methane-related BSR overlying a second BSR that could be related to a mix of heavier gas
151 (*Jatiaux et al., 2019*), (3) two different positive amplitude anomalies horizontally delimited by the
152 BSR; massive high-amplitude bodies below and vertical pipes that connect the BSR with the seafloor
153 above.

154 **3. Data and Methods**

155 This study adopts the methodology of *Serié et al. (2017)* to characterize the fluid flow phenomena in
156 the Kwanza basin. We refined it by integrating a detailed slicks inventory together with AUV-based
157 sub-bottom profiler data. Precise location of oil slicks origins at the sea surface better locates the
158 location of the active seeping vents at the seafloor (*Jatiaux et al., 2017*) and to evaluate the seepage
159 activity. In addition, the SBP provides greater discrimination between seafloor fluid-related
160 morphotypes and shallow acoustic anomalies. All the maps shown in this publication (Fig. 3a, b; Fig.
161 6a, b; Fig. 7f; Fig. 9a, b and Fig. 11 a, b) cover the exact same area (red square location in Fig. 2)
162 which has been upscaled to enhance the quality of maps although the study was conducted over a
163 larger area that corresponds to the province imaged with 3D seismic.

3.1. SAR data and seepage slicks inventory

164
165 The entire SAR collection consists of long-range monitoring integrating 156 scenes acquired over 21
166 years. The variability of the SAR acquisition data distribution is high, both temporally and spatially, as
167 seen in Table 1 and Fig. 2, respectively. The oil-seeping province is imaged with a stack of SAR scene
168 collection varying from 50 to 150 overlapping scenes (Fig. 2). The SAR dataset consists of a
169 combination of X-band (wavelength of 2.5 to 3.75 cm) and C-band (3.75 to 7.5 cm) data that are
170 known to be the most suitable wavelengths to detect oil slicks at the sea surface, enabling the
171 recognition of the thinnest oil films (*Gade and Alpers, 1998*). The oil at the sea surface reduces the
172 wind-induced capillary waves, thereby locally decreasing the radiometric values on SAR data. The
173 discrimination of look-alikes (i.e. platform or boat spill, low wind effects, algal blooms) is primarily
174 based on object features (radiometric values, edge sharpness and sinuosity), the remaining potential
175 seepage slicks database is stacked on a compilation map. The variable orientation of surface slicks
176 controlled by the sea surface water displacement (wind and currents) creates diverging patterns
177 whose centres identify the oil surfacing area (black stars in Fig. 2; *Jatiaux et al., 2017*). The proximal
178 terminations of individual slicks in the oil surfacing area are called Oil Slick Origins (*OSO; Garcia-*
179 *Pineda et al., 2010*). When there is no predominant current, the vertical projection of the average
180 location of the OSO on the seafloor provides the most accurate location of the source on the
181 seafloor.

182 **Table 1 : Inventory of SAR scenes collection characteristics.**

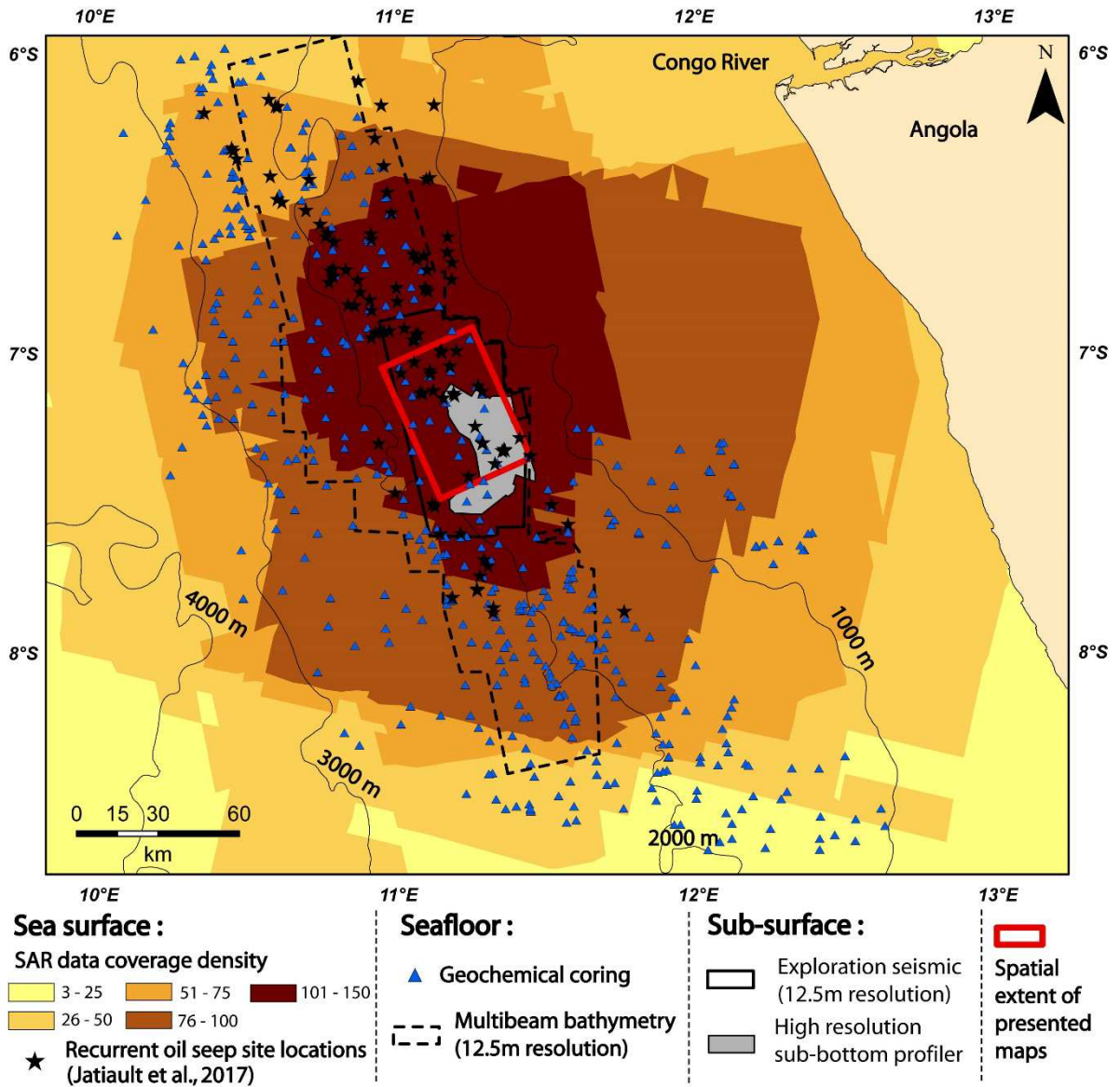
Satellite/ Sensor	Period of imagery	Wavelength	Pixel Spacing (m)	Amount of SAR data
Envisat /WSM	2002 - 2012	C (5.8 cm)	75	46
ERS/IMP	1994 - 2001	C (5.8 cm)	12.5	17
Cosmo-SkyMed	2009 - 2014	X (3.1 cm)	3-15	80
TerraSAR – X	2011	X (3.1 cm)	20	6
RADARSAT-2	2005 - 2012	C (5.3 cm)	25-50	7

183 **3.2. Geochemical coring**

184 The seafloor coring campaign was based on regional 2D seismic sections, across the deep
 185 transitional/compressive province of the LCB (blue triangles in Fig. 2). Piston cores were collected
 186 prior to the acquisition of high resolution 3D seismic presented in this paper. The entire dataset
 187 consists of 488 piston cores recovered during several coring campaigns between 1998 and 2010 by
 188 TDI Brooks. The piston cores consist of a vertical succession of 20 cm-long sub-sections with a
 189 maximum depth of 5.6 m. The geochemical analyses include:

- 190 - Gas Chromatography - Mass Spectrometer (*GC - MS*) which provides the distribution of alkane
 191 composition (S_n alkane) assessed from the retention time (performed for 423 cores out of the
 192 whole set). The sum of individual extractible alkane portions provides an estimation of the
 193 concentration of high molecular-weight hydrocarbon (C_{15+} hydrocarbon concentration).
- 194 - Unresolved Complex mixture (UCM) defined as the unextractable organic carbon with
 195 chromatogram (C_{15+}).
- 196 - Total Scanning Fluorescence (TSF) intensity measured with spectrometry technique, which helps
 197 quantify the fluorescence of aromatic components (**Abrams, 2005**). The maximum intensity
 198 (I_{max}) corresponds to the maximal values of fluorescence between emission (*EM*) spectrum and
 199 excitation (*EX*) spectrum (e.g. **Barwise and Hay, 1996**). The ratio (R_1) between maximal value of

200 EM and EX provides an indirect estimation of $^{\circ}\text{API}$ (American Petroleum Institute; API gravity = -
 201 $0.1 \cdot R_1 + 59.8$).
 202 - D



203

204 **Fig. 2: Geographical localisation of the study area and compilation of available dataset. The red**

205 **square refers to the spatial extent of maps displayed in Fig. 3a, b; Fig. 6a, b; Fig. 7f; Fig. 9a, b and**

206 **Fig. 11 a, b.**

207 3.3. Seismic dataset

208 The available seismic dataset consists of a 3D seismic cube used for petroleum exploration,
 209 complemented by a high-resolution survey used for geo-hazards evaluation acquired with an
 210 Autonomous Underwater Vehicle (AUV).

211 **Table 2 : Characteristics of the available datasets including seafloor and sub-seafloor imagery.**

Data type		Line spacing (m)	Maximum Penetration (ms TWT)	Dominant frequency	Horizontal Resolution	Vertical Resolution	Covered area
Sub-seafloor	3D exploration seismic	12.5*12.5	4500	20 - 100 Hz	12.5 m	~4 m	3300 km ²
	AUV Sub-bottom profiler	175*1000	100	1.5 - 4.5 kHz	1.5 m	~10 cm	5500 km ²
Seafloor	Multibeam	-	-	12.5 kHz	12.5 m	-	16 000 km ²
	AUV HR bathymetry	-	-	200 kHz	1.5 - 3 m	-	830 km ²
	AUV Seafloor Reflectivity	175*1000	Few centimetres	120 - 410 kHz	3 m	-	830 km ²

212 The seismic cube covers a 3300 km² area with a maximum record length of 4500 ms TWT (Fig. 2). The
 213 source system is composed of two airgun clusters, 50 m separated with shot interval of 25 m. The
 214 sensor system consists of 10 parallel, 100 m separated streamers, and composed of 396 individual
 215 receiver groups separated by 25 m. We used the near-offset seismic trace.

216 The Sub-Bottom Profiler (SBP) dataset followed a grid with a line spacing of 1000m in the slope
 217 direction and 175m in the strike direction, and was acquired in two surveys operated in 2009 by C&C
 218 and in 2011 by Fugro (Table 2). The combination of the two datasets consists of an 830 km² gridded
 219 area and 5500 km of SBP sections. The high-frequency SBP is characterised by a 10 cm vertical
 220 resolution whereas the penetration is limited to the first 100 ms TWT below seafloor. We used the
 221 amplitude attribute to display the 3D seismic impedance contrast at lithological interfaces. The RMS
 222 (Root Mean Square) amplitude was used to display SBP sections and to identify geophysical
 223 anomalies on 3D seismic. Seafloor curvature maps are computed from the first arrivals of the 3D
 224 seismic cube, using a window size of 3 profiles and an interpolation length of 5 samples.

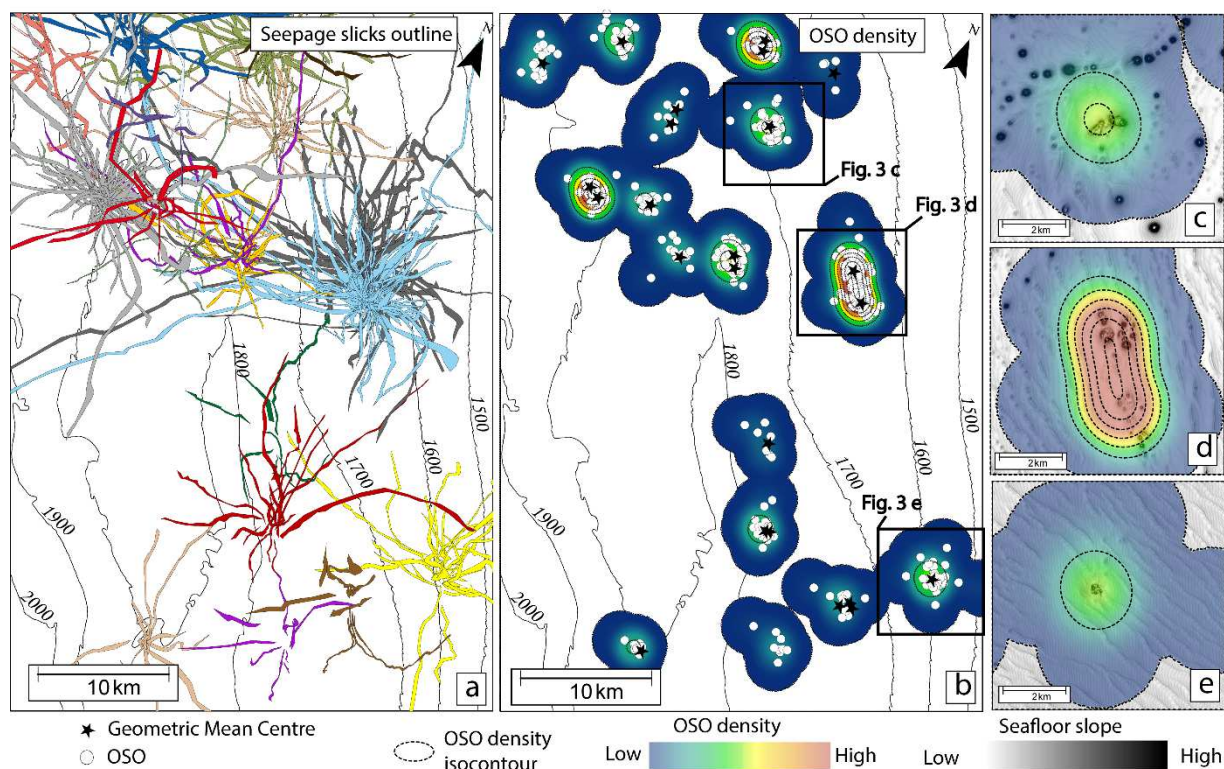
225 The high-resolution survey includes bathymetry (EM2000 multibeam echo-sounder) and seafloor
226 reflectivity acquired along the acquisition tracklines of the vehicle. In areas not surveyed by the AUV,
227 lower-resolution seafloor data (bathymetry, seismic amplitude) were taken from the seafloor
228 reflections picked on the 3D seismic using Sismage software (*Guillon and Keskes, 2004*). In addition,
229 the seafloor origin of a large majority of (>80 %) of recurrent oil seep sites were imaged at large scale
230 (16 000 km²), 12.5m resolution multibeam bathymetry. The computation of the slope map with
231 superimposed seafloor isochrones enhances the imagery of seafloor features. Seafloor curvature
232 maps are computed from the first arrivals on the seafloor, extracted from the 3D seismic cube using
233 Sismage software and taking estimation window size of three samples and an interpolation length of
234 five samples.

235 **4. Analyses and results**

236 **4.1. Evidence of active oil seeps**

237 **4.1.1. Sea surface manifestations of oil presence**

238 The visual analysis of the 156 SAR scenes revealed more than 3000 seepage slicks characterised by
239 elongated/curvilinear trends with variable length (Fig. 3a). Diverging black streaks and OSO
240 concentration area within point clusters were used to identify active oil seep sites. The oil seepage
241 system consists of more than 100 seep sites distributed on the deep part of the Miocene Congo
242 deep-sea fan for water depths between 1200 to 2700 m. Observations of multi-temporal oil slicks at
243 the sea surface vary from 5 to 80 % from one seep site to another. The radius of the spatial scatter of
244 OSO for individual sea bottom seepage points has a mode radius of 750 m (*Jatiaux et al., 2018*),
245 suggesting that the lateral deflection due to underwater currents remains low compared to the
246 water depth (Fig. 3b; *Jatiaux et al., 2019, Part I*). The vertical projection of OSO locations, the
247 density and the geometric mean centre coincide vertically at 98 % with seabed morphological
248 anomalies, confirming the absence of permanent deflection in the water column, which helps to
249 identify active oil seep sites nearly at the apex of OSO locations (Fig. 3c, d, and e).



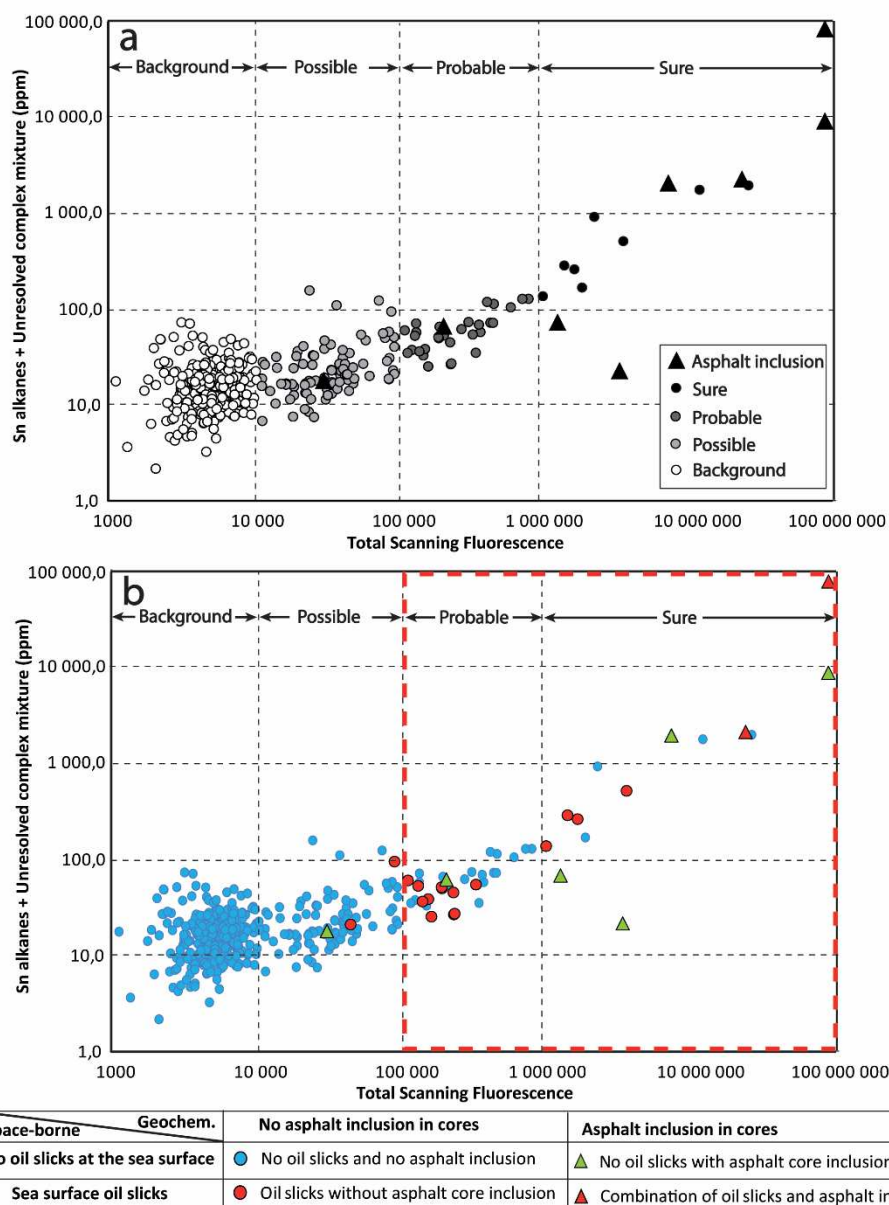
250

251 **Fig. 3: a. Compilation map of seepage slick outlines identified from the interpretation of 156**
 252 **overlapping SAR scenes. The colour corresponds to distinct active oil seep sites. b. Compilation of**
 253 **OSO pinpointed from diverging recurrent slicks in white dots, superimposed with the OSO density**
 254 **map and iso-contour. High values in warm colours correspond to frequent oil surfacing areas. c, d,**
 255 **e. Details of the OSO density map at frequent oil surfacing locations, superimposed in transparency**
 256 **with slopes map of the seafloor.**

257

4.1.2. Seafloor geochemical coring

258 The hydrocarbon content of seafloor piston cores is strongly variable (Fig. 4a). Geochemical analysis
 259 of heavy (C_{15+}) hydrocarbons shows that the sum of alkane (S_n) concentration ($C_{16} - C_{32}$) ranges from
 260 0.1 to 36 ppm while the concentration of UCM varies from 2 to 85 000 ppm. While the fluorescence
 261 (TSF) intensity changes from 1 116 to 87 240 000, 35 % of the cores have greater values than the
 262 regional background defined at 10 000 units (*Serié et al., 2017*). The plot of fluorescence vs. C_{15+}
 263 concentration is an indirect method for quantifying the presence of heavy hydrocarbons in sub-
 264 surface sediments (Fig. 4a).



265

266 **Fig. 4: a. Graph (logarithmic scale) of the concentration of the high molecular-weight hydrocarbons**
 267 **(C₁₅₊) compared to the maximal intensity of the Total Scanning Fluorescence (TSF I_{max}); the circles**
 268 **colours reflects the uncertainty on the presence of hydrocarbons in cores. b. Same graph with**
 269 **color-coded symbols to show the correlation with sea-surface slicks; symbols are classified into 4**
 270 **categories depending on the geographical correspondence of oil at the sea surface (red circles) and**
 271 **visual inclusion in cores (triangles). The red dashed rectangle delimits the two categories "Sure"**
 272 **and "Probable" that we consider reliably contain oil traces.**

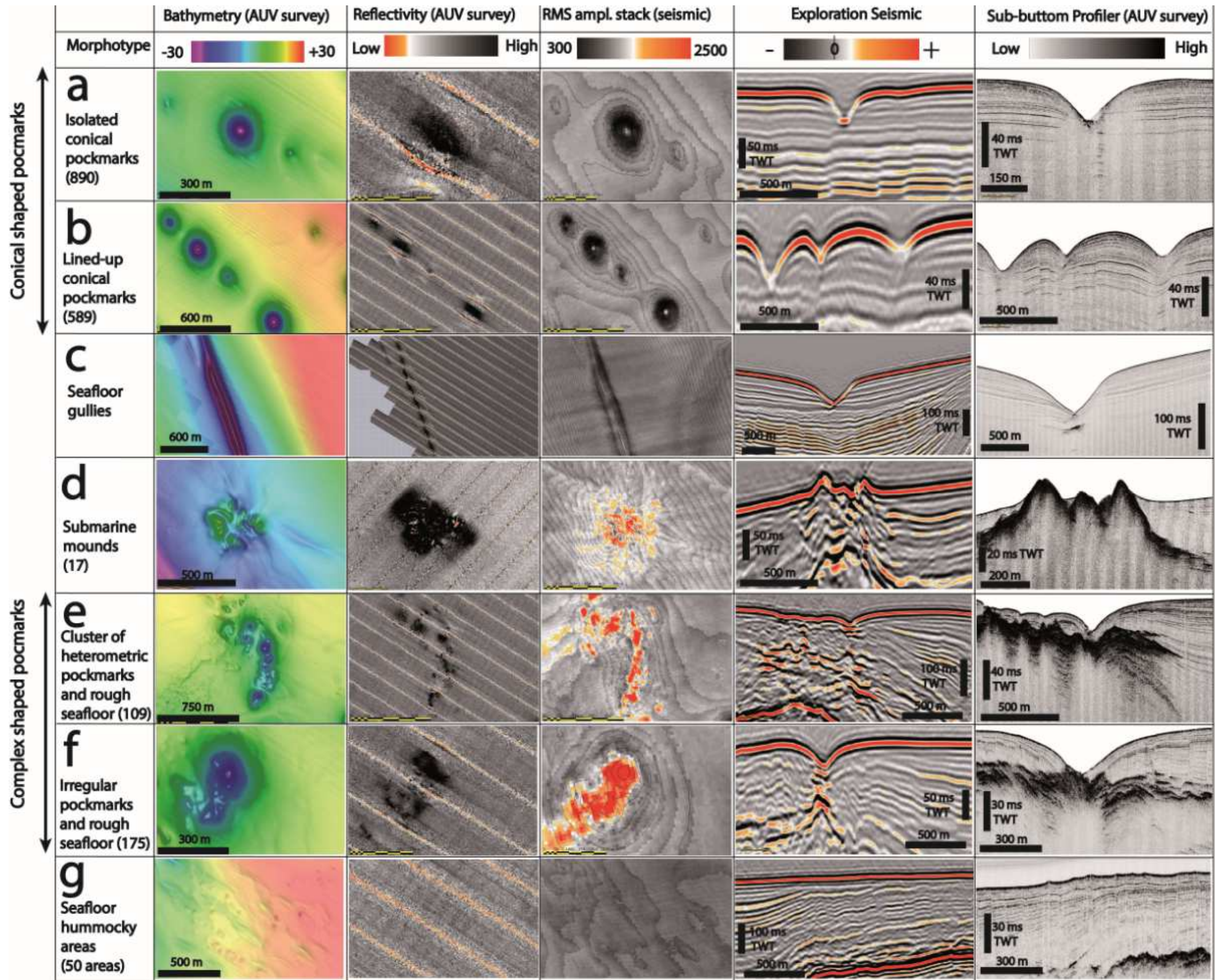
273 We considered that hydrocarbon traces are reliably present in cores for TSF values at least 100 times
274 greater than the regional background (Levaché, pers. com). Occurrence of hydrocarbons is possible
275 for 114 cores (TSF values less than 100 000, Fig. 4a). For 38 cores, hydrocarbon traces are probable
276 when the TSF intensity is at least 10 times greater than the regional background ($100\,000 < \text{TSF} <$
277 $1\,000\,000$). The presence of hydrocarbon is qualified as being sure for 20 cores having TSF values
278 greater than 10^6 .

279 The observation of asphalt inclusions for 10 piston cores also confirms the migration of oil towards
280 the seafloor (black triangles in Fig. 4a). Even if they represent only 2% (10/488) of the total core
281 array, they correspond to the highest TSF and UCM values.

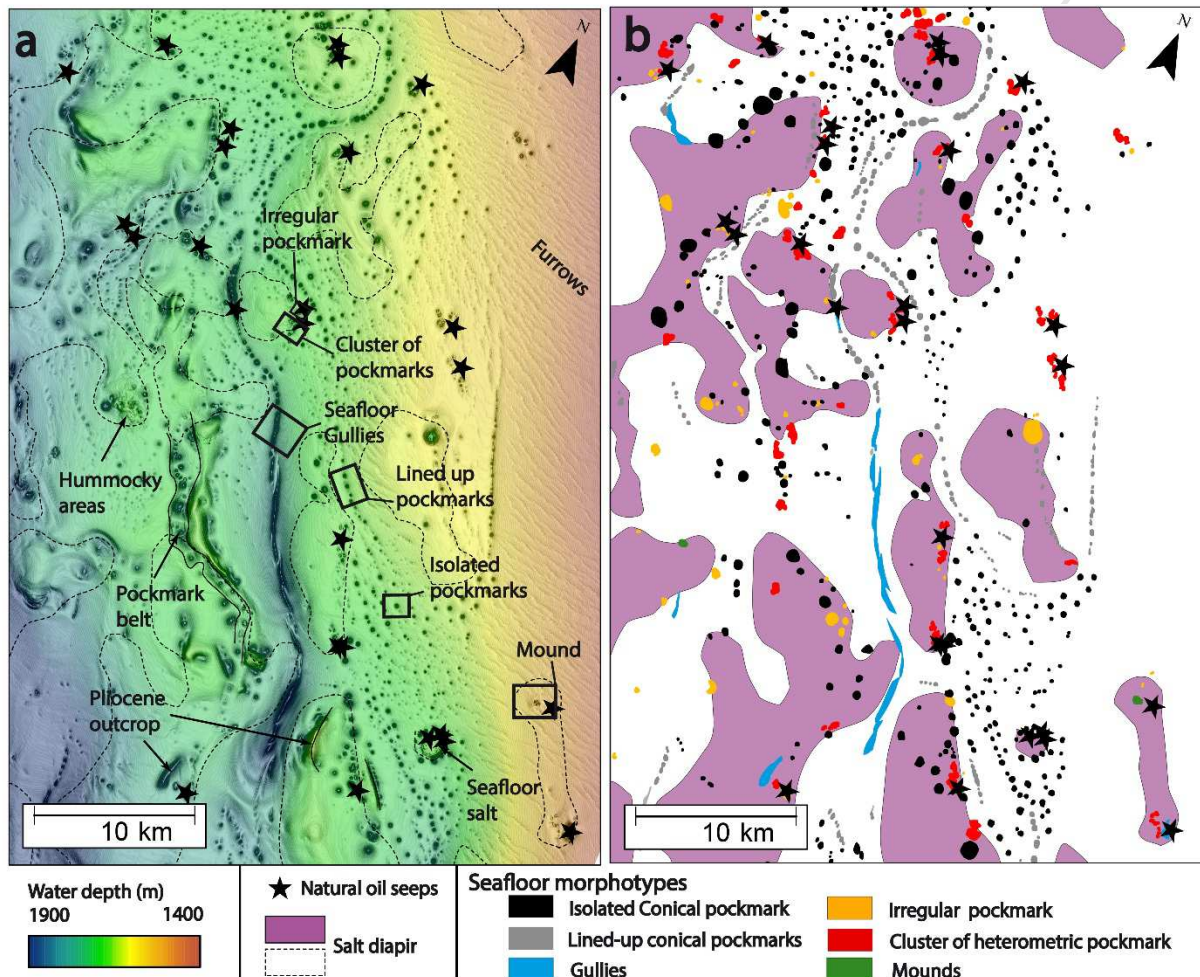
282 **4.2. Fluid flow features on the seafloor**

283 Seafloor features that may be related to fluid venting are categorised into 7 main families: conical
284 pockmarks (isolated and lined-up), seafloor gullies, complex-shaped pockmarks (clusters of
285 heterometric pockmarks and irregular isolated pockmarks), submarine mounds and scattered
286 positive topographic hummocky features (Fig. 5).

287



289 Fig. 5: Compilation of major fluid vents morphotypes observed on the seafloor in the Lower Congo
 290 Basin. The bathymetric colour scale was normalised with a 60 m dynamic range to better
 291 distinguish the different morphologies. High amplitudes are displayed in black on the reflectivity
 292 map and in red on the seafloor amplitude extracted from 3D seismic.



293
 294 Fig. 6: a. Map of the seafloor (dip + isochron) showing the distribution of fluid flow features. b.
 295 Interpretative map of focused fluid flows sorted according to their morphotypes. Black stars show
 296 the positions of the mean impact points of oil slicks at the sea surface.

297 4.2.1. The conical pockmark-gully continuum

298 Conical pockmarks can reach km-scale diameters with maximum depth of 150 m and are
 299 characterized by gentle slopes of $\sim 15^\circ$ (Fig. 5a). With a total number of 890, they are widespread
 300 throughout the study area and mostly occur in salt minibasins (Fig. 6).

301 Lined-up conical pockmarks (Fig. 5b), defined as a succession pool of at least 3 conical pockmarks
302 along a main direction, occur in 3 main settings. First, they are sparsely distributed along the maximal
303 flexural axis of salt minibasins (Fig. 6). Increase of their number and density can ultimately lead to
304 form curvilinear gullies (Fig. 5c) corresponding to deep (>50 m) and elongated (> 1 km) incised
305 depressions on the seafloor. Second, conical pockmarks can occur at the tip of normal faults on the
306 seafloor in association with the sagging of minibasins. Third, they are located at the seafloor interface
307 unconformity between uplifted slabs of Miocene-Pliocene series at diapirs and Quaternary siltstones
308 in minibasins. The total amount of conical pockmarks, including isolated ones and aligned sets, is
309 significant in the study area (1 750 individual features) (Table 3), which represents 85% of the total
310 fluid escape features identified on the bathymetric data.

311 **4.2.2. Submarine mounds**

312 Submarine mounds are bathymetric highs on the seafloor with a typical relief of 5 to 20m above the
313 surrounding seabed and diameter up to 500m (Fig. 5d). We identified only 17 such mounds; the only
314 one of these that is imaged on HR data appears as a cluster of smaller individual mounds, whose
315 slopes range from 10 to 30°. The high-resolution bathymetry map reveals fault sets diverging radially
316 away from the seafloor mounds; similar radial patterns have been observed around salt diapirs by
317 **Carruthers et al. (2013)**. Submarine mounds are clearly discernible on the seafloor as patches with
318 higher reflectivity compared to the surrounding seabed, indicating that they are formed of higher
319 impedance material than the background silts and clays. Seafloor mounds are located above
320 allochthonous salt diapirs like the irregular pockmark clusters (Fig. 5). Most of the submarine mounds
321 are associated with spiky diapirs (needle-shaped salt protrusion), and have not been observed above
322 bulbous ones. No clear distinction in terms of seepage proficiency (occurrence rate) could be
323 established between submarine mounds and other active features.

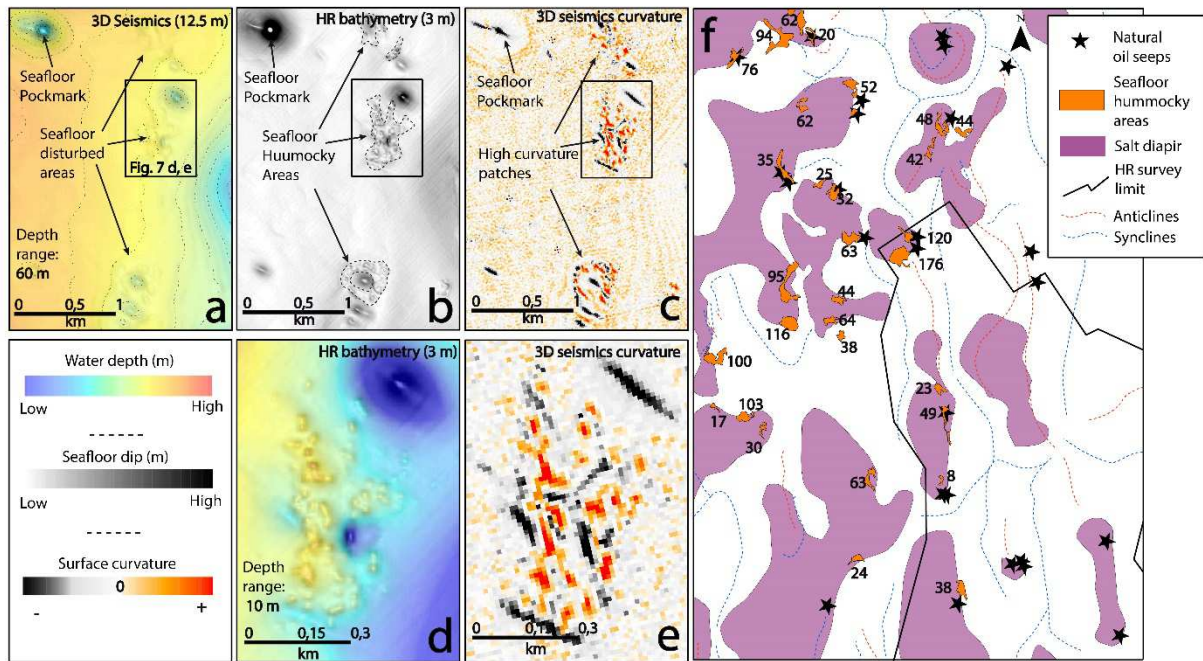
324 **4.2.3. Complex shaped pockmarks**

325 Complex-shaped pockmarks are uneven fluid escape features on the seafloor with a main depression
326 whose depth does not exceed a few tens of meters. Complex-shaped pockmarks occur as two

327 distinctive patterns; (1) Clusters of heterometric pockmarks (Fig. 5e), defined as an aggregation of a
328 large number of unit pockmarks (*Hovland et al., 2010*), with clusters reaching 2-3 km and exceeding
329 1500m in length (*Jatiault et al., 2019, Part I*). They usually develop along the salt-related fault
330 networks at the rim of a salt canopy, thereby creating a complex-shaped depression at broader scale,
331 that contains different heterometric pockmarks; (2) Irregular pockmarks (Fig. 5f), corresponding to
332 sub-circular depressions with a rough aspect at the base. Local depressions are associated with a
333 strong high-amplitude anomaly on the seafloor reflectivity map (Fig. 5). In contrast with previously
334 described mounds, they are mostly found along landward flanks of bulbous diapirs, and never appear
335 in association with spiky ones. We identified 109 clusters of heterometric pockmarks and 175
336 irregular isolated pockmarks.

337 **4.2.4. Seafloor hummocky areas**

338 The seafloor is affected by rough patches clustering over limited-size areas (10-15m in diameter and
339 few meters high), on top of salt diapir. They were identified on high-resolution bathymetry maps and
340 therefore remain below the 3D seismic resolution (Fig. 7a). However, seafloor hummocky induces a
341 slight disturbance in the seafloor creating a rough aspect that may be discernible from the
342 exploration seismic resolution using specific seismic attributes such as seabed curvature (Fig. 7a). On
343 the HR bathymetry, hummocky areas consist of a numerous small hummocks (Fig. 7b). The
344 discrimination of hummocky features is particularly enhanced using the curvature attribute that
345 measures the bathymetric slope inflexions (Fig. 7c). On curvature maps, hummocky features are
346 characterised by a central (round or elongated; Fig. 7d) high positive value over topographic features,
347 surrounded by sub-circular medium values (~ 0) and by negative values at the rim (Fig. 7e).



348

349 **Fig. 7: a. Seafloor map from 3D seismic, the dynamic range of the seafloor colour scale is 60 m. b.**
 350 **Seafloor slope map of the 3m resolution multi-beam echo sounder affected by the meter-scale**
 351 **seafloor hummocky areas. c. Curvature map of the seabed from the 3D seismic data. d. Zoom of**
 352 **the 3m resolution echo-sounder seafloor map (bathymetric range is 10 m) superimposed with the**
 353 **slope map. e. Zoom of the seabed curvature map from the 3D seismic data. f. Geographical**
 354 **inventory of the hummocky areas superimposed with salt diapir locations and natural oil seep**
 355 **sites. The numbers refer to the amount of detected individual hummocks.**

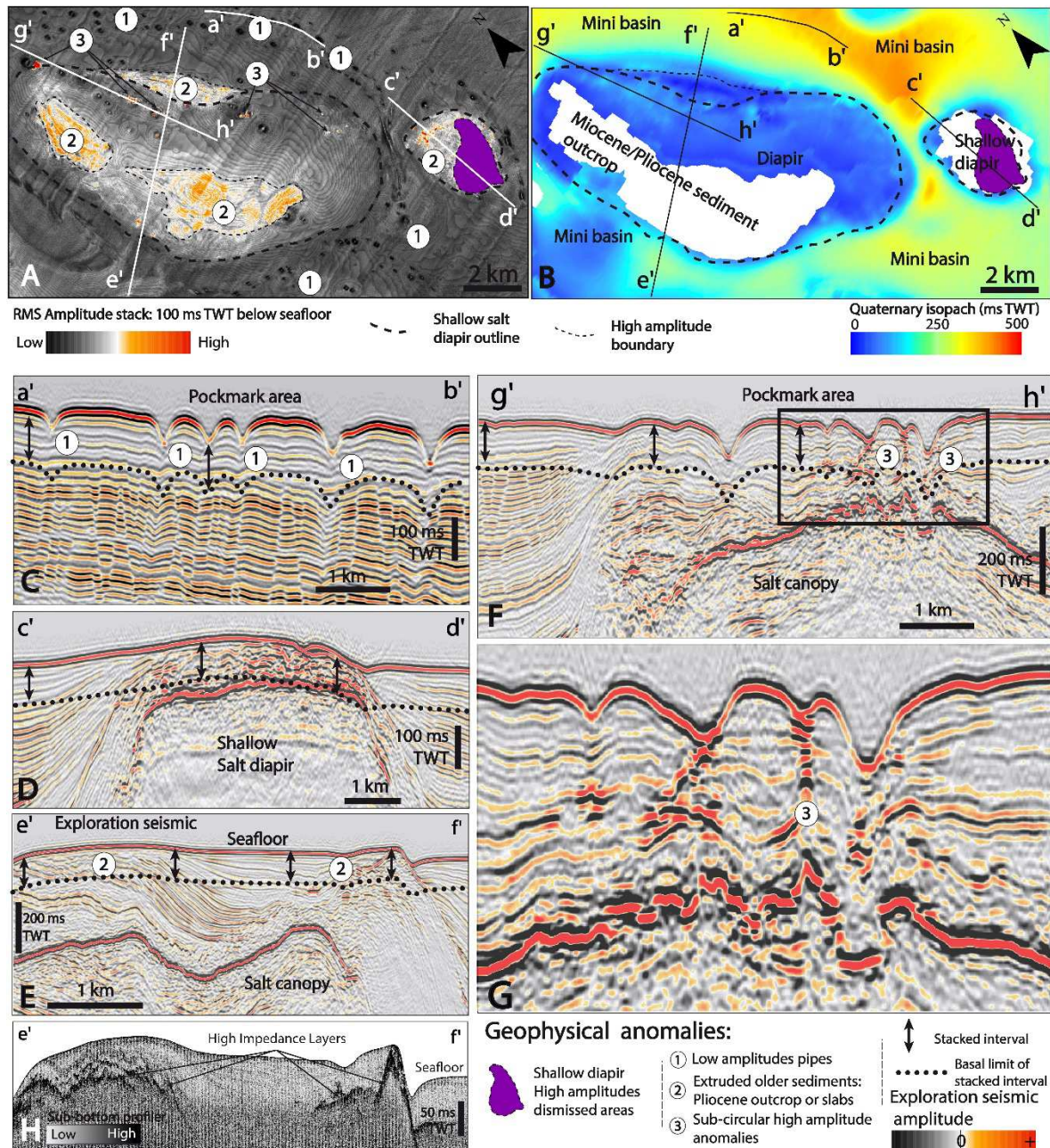
356 We assumed that rough patches correspond to zones with a high density of seafloor hummocks and
 357 individual positive sub-circular features correspond to individual hummocks. The presence of
 358 hummock clusters is associated with complex-shaped pockmarks (clusters of heterometric and
 359 irregular pockmarks) in most cases. Underlying HIL remains buried under few tens of ms below the
 360 seafloor and connected to hummocks by shallow faults (Fig. 5g). We identified 2946 possible
 361 individual hummocks over the area imaged with 3D seismic. Ten areas with a high hummock
 362 concentration were identified on the HR survey and an additional 50 on the wider 3D survey (12.5m
 363 resolution) (Fig. 7). 3D seismic data detects about 55% of individual hummock features visible on the
 364 HR survey. The number of discernible hummock features in clusters ranges between 10 to 210 on the

365 3D seismic, covering surface areas from 0.12 to 3.45 km² and corresponding to a density of 35 to 240
366 hummocks per km². One piston core was drilled inside a hummocky cluster visible on the 3D seismic
367 and showed asphalt inclusions in the sediment. Hummocks have the same morphology and
368 geophysical characteristics as asphalt mounds and their distribution is similar to that of those
369 previously identified in the area (*Unterseh et al., 2013; Jones et al., 2014*). Seafloor hummocks are
370 interpreted as seafloor asphalt storage that reached the seafloor through scattered emission points
371 above the crest of salt diapirs, following a stage of oil migration across sedimentary series.

372 **4.3. Seismic geomorphology in the sub-surface**

373 *4.3.1. Positive geophysical anomalies on the 3D seismic*

374 We computed the RMS amplitude stack of the first 100 ms TWT below the seafloor reflection to
375 identify geophysical anomalies (Fig. 8 A). Geophysical anomalies occur as three main distinct
376 features, or categories.



377

378 **Fig. 8: A. Map of amplitude root mean square (RMS) over the first 100 ms TWT below seabed,**
 379 **showing four types of seismic anomalies. The dotted ellipse is the outline of a shallow diapir that**
 380 **coincides with consistent high amplitudes close to the seafloor, the outcrop of Neogene series that**
 381 **creates a moderate amplitude anomaly, the sub-circular low amplitude anomaly in minibasins and**
 382 **smaller sub-circular high-amplitude anomalies associated above salt diapirs. Please note that the**
 383 **North arrow has been rotated to ensure optimal visibility. B. The quaternary sediment isopach**
 384 **reveals the differential sedimentation between minibasin area and diapir area. C, D, E, F. Seismic**

385 sections through the different geophysical anomalies identified on fig. 8A (see details in text and
386 locations on the Fig. 8 A, B). G. Zoom of from section F on high-amplitude pipes. H. SBP section
387 across the High Impedance layer.

388 Above shallow salt diapirs, the RMS interval cross-cuts the top of salt, making high-amplitude
389 anomalies that are unrelated to fluid effects. We dismissed these areas from the interpretation
390 (purple patches in Fig. 8).

391 The first type of acoustic anomaly (1 on Fig. 8 A) is defined as a vertical succession of low-amplitude
392 reflections. Low-amplitude pipes suggest acoustic dimming in the sedimentary pile where the
393 impedance contrasts are attenuated across successive lithologic interfaces. Low-amplitude pipes are
394 essentially spread across salt minibasins or aligned along the maximal flexural axis of salt minibasins
395 (Fig. 8 A; Fig. 9). We identified a large number of low-amplitude pipes (582) across the area imaged
396 using the exploration seismic (Fig. 9). The low-amplitude anomalies identified on the 3D seismic
397 correspond to the locations of conical shaped pockmarks (isolated and aligned) and gullies (Fig. 8 C).
398 The lithologic interfaces are disrupted by an acoustically transparent zone in the sub-bottom profiler
399 below the location of conical pockmarks (Fig. 5). Lithologic interfaces are either truncated by the
400 seafloor depression or associated with a slope inflection, stacked on successive lithologic interfaces.
401 In the former case, the active fluid seep probably corresponds to a recent initiation of the seepage
402 activity. In the latter case the deepest interval affected can be followed down to 600 ms TWT on the
403 exploration seismic. On the sub-bottom profiler, stratigraphic boundaries surrounding the low-
404 amplitude anomalies remain well organised down to the acoustic penetration. Most correspond to
405 the bulls-eye pockmarks defined by *Andresen et al. (2011)*.

406 The second type (2; Fig. 8 A) of acoustic anomaly corresponds to moderate positive amplitude
407 anomalies related to outcropping older sediments (mostly Neogene) above salt diapirs; these
408 anomalies gradually dim out laterally (Fig. 8 E). Affected areas range from 1 to 10 km². Moderate
409 amplitude anomalies are composed of consistent, extensive patches indistinctively downslope or

410 upslope (Fig. 8 E) in relation to the depocentre shift/tectonic inversion (**Quirk and Pilcher, 2012**).

411 Uplifting of older sediments can also be detected on the sub-bottom profiler sections where they

412 occur as strong threadlike reflections (Fig. 8 F).

413 The third type (3; Fig. 8 A) of acoustic anomaly corresponds to local, sub-circular and Positive High

414 Amplitude Anomalies (PHAA; **Ho et al., 2012**) that are vertically stacked on successive lithologic

415 interfaces, marking a vertical succession of strong impedance contrasts (bright anomalies; Fig. 8 G).

416 The PHAA diameters vary from 60 to 350m and occur either as multiple vertical pipe clusters (see

417 **Jatiault et al., 2019, Part I**) or isolated chimneys (Fig. 8 G). We identified 75 individual PHAA on the

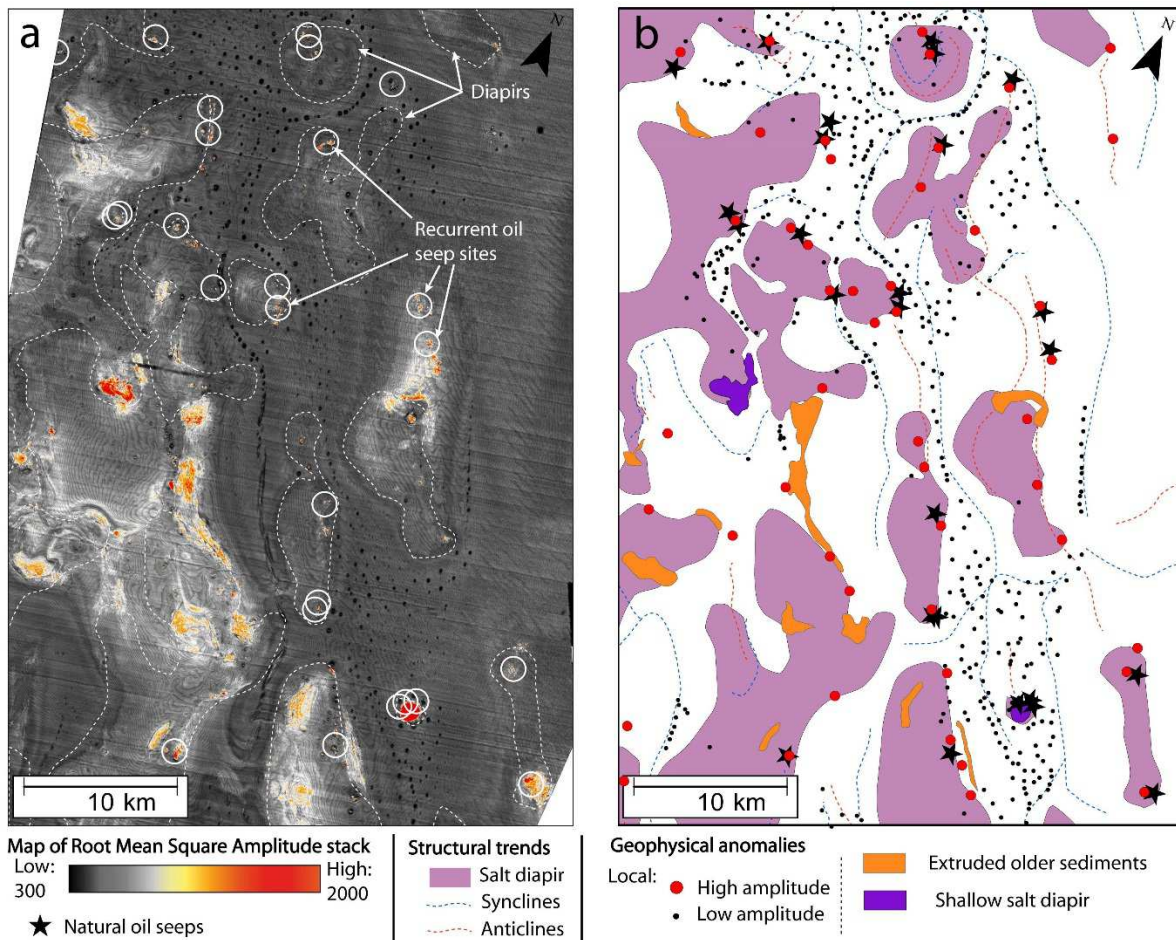
418 RMS amplitude stack of the first 100 ms TWT, mostly associated with diapirs (Fig. 9). They tend to

419 congregate along the upslope salt flank or minibasin edges. High-amplitude vertical pipes are mostly

420 associated with strong RMS amplitude in the central area surrounded by a moderate amplitude

421 peripheral anomaly. The seafloor expression of PHAA corresponds essentially to the complex shaped

422 pockmarks (clustered or isolated) and submarine mounds.



423

424 **Fig. 9: a. Map of the RMS amplitude stack of the first 100 ms TWT below seafloor. Geophysical**
 425 **positive amplitude anomalies are visible as warm colours. White circles show the average surfacing**
 426 **areas of recurrent oil seeps. b. Map of the allochthonous salt represented as purple polygons. The**
 427 **anticline/syncline of the Late/Early Pliocene transition is displayed as red and blue dashed**
 428 **polylines, respectively. The geophysical anomalies extracted from the RMS amplitude stack are**
 429 **categorised into four main families: shallow salt diapir, exhumed older and compacted sediments,**
 430 **pseudo-circular amplitude diming and vertical stack of pseudo-circular high-amplitude anomalies.**

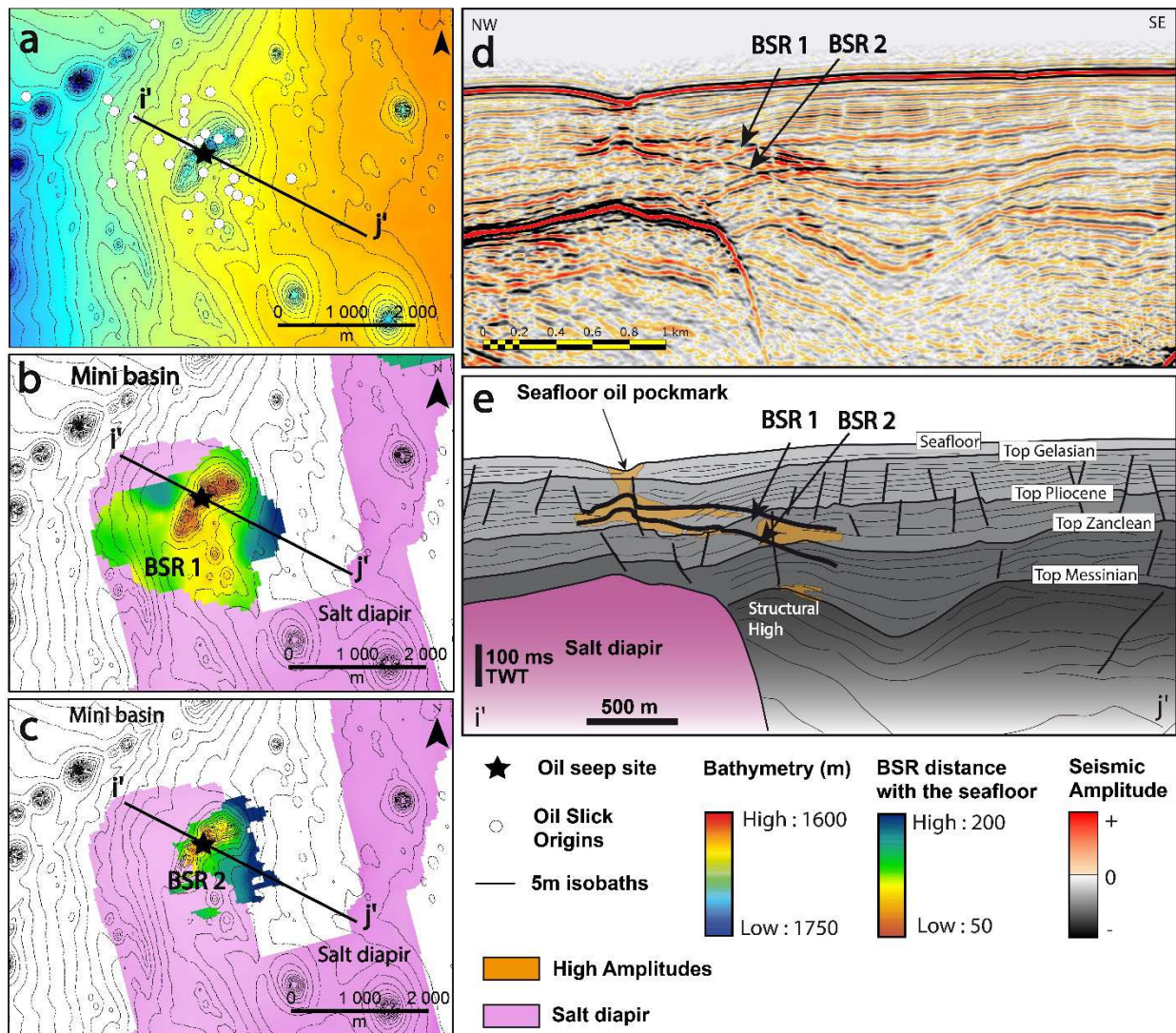
431 **4.3.2. Negative polarity reflections**

432 Occasionally, consistent negative reflections crosscut stratigraphic series with all the characteristics
 433 of a methane hydrate BSR. The BSR occurs as extensive reflectors in minibasins with a distance from
 434 the seafloor ranging roughly from 250 to 500 ms TWT and is usually underlain by a thick High-
 435 Reflectivity Zone (**Andresen et al., 2011**).

436 Approaching the salt diapirs, the BSR shoals up to a range of 50 to 250 ms TWT below the seabed; it
437 generally occurs in discrete small patches (Fig. 10a). This difference between the overburden of the
438 diapirs and minibasins is known to be associated with the high thermal conductivity of the salt, which
439 concentrates heat above diapirs, resulting in a higher geothermal gradient there, and consequently a
440 thinner hydrate stability zone (*Lucazeau et al., 2004*). The BSR corresponds to the basal limit of pipe-
441 like features (type 3 anomalies) characterised by a vertical succession of PHAA and is underlain by a
442 100 ms-thick high-amplitude interval.

443 The sub-surface series are also locally affected by an occasional second negative polarity reflection.
444 The horizon occurs as a continuous, crosscutting surface and tends to be parallel to the first BSR. The
445 vertical distance with the BSR is mostly constant (~50ms), or occasionally increases towards the
446 minibasins (Fig. 10). The thermal effect associated with the presence of a salt diapir also affects the
447 vertical location of the second BSR by decreasing the distance from the seafloor. Double BSRs are
448 observed exclusively above salt diapirs. Both BSRs are concomitantly and locally deflected upward
449 below seafloor depressions, which also correspond to the locations of PHAA (Fig. 10).

450



451

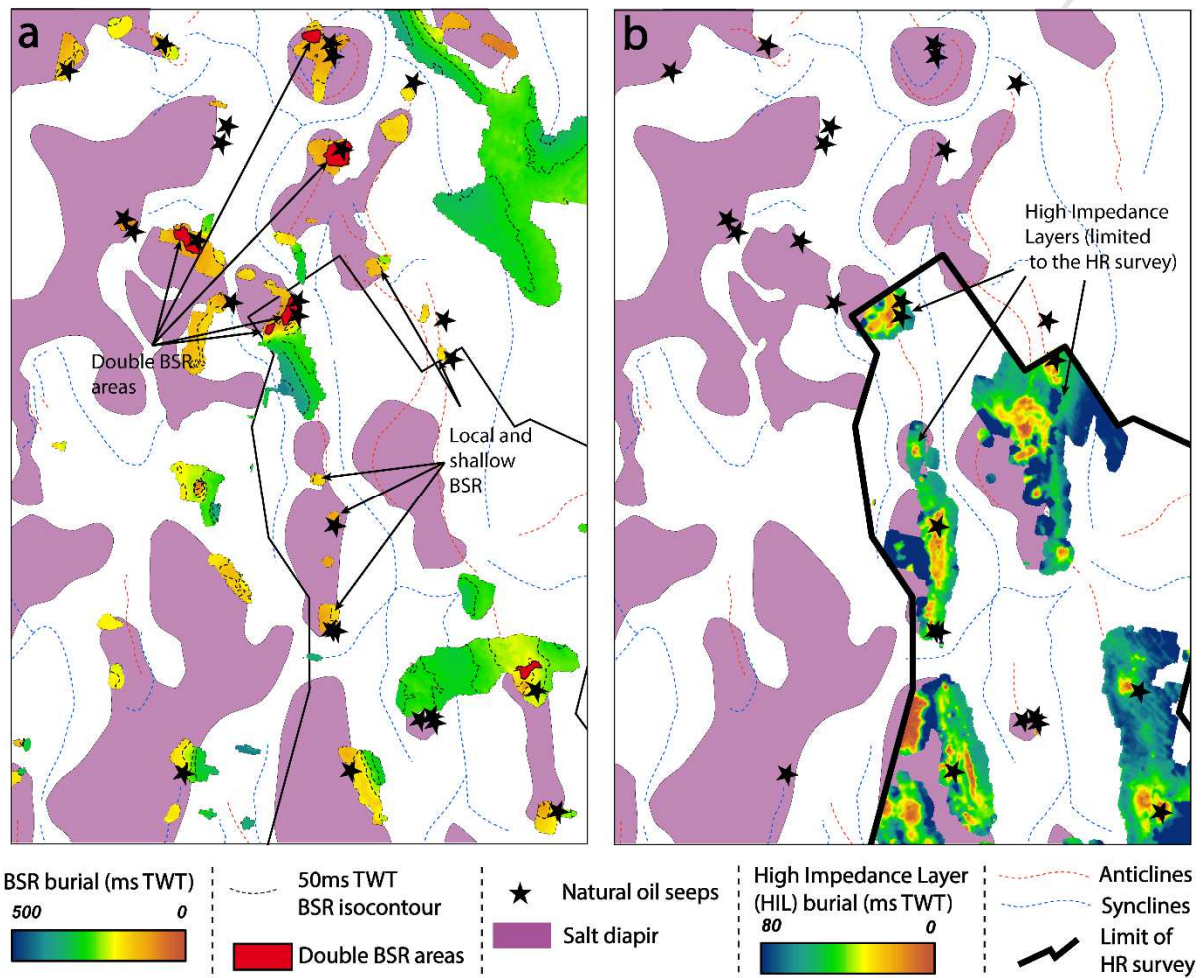
452 **Fig. 10: a.** Seafloor map superimposed with 5m isobaths, oil slick origins (OSO; Garcia-Pineda et al.,
 453 2010) and location of oil seeps identified with the SAR system. **b.** TWT difference map between
 454 upper BSR and seafloor, superimposed with the extension of the underlying diapir and 5m
 455 isobaths. **c.** TWT difference map of the lower BSR with the seafloor, superimposed with the
 456 underlying diapir extension and 5m isobaths. **d.** Seismic section across a double BSR marked by
 457 two stacked black horizons (see location in Fig. 10.a) **e.** Interpretative line drawing.

458

4.3.3. Subsurface high impedance layer

459 A consistent High-Impedance Layer (HIL) frequently appears on sub-bottom profiler sections, in the
 460 shallow sub-surface above the salt diapirs (Fig. 8 H). HIL are only identified on the high-resolution
 461 survey and consist of a high-amplitude cross-cutting reflector. High-Impedance Layers occur in

462 patches whose surface areas can reach 120 km², the average being 20 km² (Fig. 11 b). They are
 463 located above diapiric areas, mostly at the upslope flank but can also be occasionally found
 464 downslope. The TWT difference with the seafloor ranges from 0 to 80 ms TWT above diapirs and can
 465 be higher (up to 200 ms TWT) in minibasins.



467 **Fig. 11 : a. Extract of the Bottom Simulating Reflection (BSR) map with basin structure in**
 468 **background illustrating the relationship with hydrate and oil seep sites. b. Isochron map of the HIL**
 469 **in the shallow sub-surface from sub-bottom profiler data. The colour scale displays the distance**
 470 **between the seismic horizon and the seafloor.**

472 5. Synthesis and discussion

473 5.1. Integrative synthesis of the oil seepage situation

474 A subset of 22 cores spatially corresponds to the vertical projection of recurrent oil seep sites
475 detected from the SAR study, within a radius of < 1500 m (red dots and green triangles in Fig. 4b).
476 Geochemical analyses were successfully performed for 19 out of 22 cores. For these sampled oil seep
477 sites, the C_{15+} concentration (Sn Alkanes + UCM) shows high concentrations of heavy hydrocarbons
478 and TSF values at least 50 times higher than the regional background. A large majority (17/19) of
479 sampled oil seep sites fall into the "Probable" and "Sure" categories and the remaining (2/17) into
480 the "Possible" category (red dots and green triangles in Fig. 4b). These observations validates the
481 assumption that lateral drift in the water column averages to nil over time and confirms that, without
482 any systematic offset, the pockmarks beneath the barycentre of OSOs corresponds to the source of
483 expelled oils, on a regional scale as demonstrated from integration of vertical mooring data (*Jatiaux*
484 *et al., 2018*). Considering that 58 pistons belong to the "Probable" and "Sure" categories, 38%
485 (22/58) correspond to the location of recurrent seepage slicks detected with the SAR system. The oil
486 gravity, estimated using the fluorescence technique, ranges from 10 to 40°API for active oil seep sites
487 associated with sea surface manifestations of oil.

488 Even though visual confirmation of asphalt inclusion remains uncommon (10 cores; black triangles in
489 Fig. 4a), 40% of drilled sites showing asphalt inclusions (4/10; green triangles in Fig. 4b) are located
490 close to a recurrent seep site at the sea surface. The geochemical analysis is available for 2 cores
491 associated with asphalt inclusions and shows that the TSF values and the concentration in C_{15+}
492 reaches the highest values in the core dataset (Fig. 4b).

493 We identified multiple fluid-related morphotypes on the seafloor in our study area (Fig. 5). Let us
494 examine which ones can be considered characteristic of oil-bearing seeps compared to other fluid
495 releases, by comparing geophysical features against the results of the SAR study. The number of
496 conical pockmarks, including aligned and isolated cones, represents 85% of the total fluid escape

497 features identified on the bathymetric data (1 750 individual features) (Table 3). Although these
498 features are abundant, none are presently responsible for oil seepage detected with SAR systems.
499 Conversely, clusters of heterometric pockmarks, irregular pockmarks and submarine mounds are
500 occasional across the margin. Respectively, 109, 175 and 17 were indexed from bathymetric
501 analyses, making barely 15 percent of the total number of identified seafloor fluid-escape features.
502 These 15 percent account for 98% of seafloor vents responsible for oil supply during the observation
503 period (Table 3).

504 Seafloor hummocky areas are associated with oil slicks detected with SAR data for 5 out of the 10
505 seafloor hummocky areas detected on the HR dataset and 21 out of the 50 identified from the 3D
506 seismic. Both the HR survey and information deduced from 3D seismic suggest that barely half of
507 asphalt mounds fields are associated with detectable and recurrent slicks at the sea surface (21 out
508 of entire 50 hummocky areas array).

509 On the subsurface, the area imaged with the 3D seismic covers 30 individual recurrent oil seep sites,
510 28 of which are either directly related to shallow salt diapirs, or correspond to the outcropping older
511 sediment slabs uplifted by differential salt movements. The seafloor origin of recurrent oil seep sites
512 visible exclusively on SAR data (100 %) corresponds to PHAA pipes in the shallow subsurface
513 (<100ms; Fig. 9). Among the 75 individual vertical pipes identified (type 3; Fig. 8 A), about 40% of
514 geophysical anomalies (30/75) are currently associated with prolific seep sites. Conversely, none (0%)
515 of low amplitude pipes identified across the study area are associated with oil seeps visible on space-
516 borne data. Among the 75 local positive geophysical anomalies (type 3) recognised using the 3D
517 seismic, about 60 % (45/75) are associated with a BSR. Among the 30 recurrent oil seep sites imaged
518 with 3D seismic, 21 (70 %) are emplaced directly above a shallow BSR. Double BSR are unusual in the
519 study area but exclusively occur to oil seep sites detected with the SAR system (see red patches in
520 Fig. 11 a). Six of the 30 recurrent oil seep sites detected with the SAR system and imaged with 3D
521 seismic are directly emplaced above a double BSR. All the detected oil seeps belong to the areas
522 associated with the development of a HIL (Fig. 11 b). Moreover, the interpreted seafloor origin of oil

523 seeps (irregular isolated pockmarks and cluster of heterometric pockmarks; Fig. 5) corresponds to
 524 areas where the HIL reach the seafloor. There is a strong geographical correlation between seafloor-
 525 reaching HIL, shallow local BSR and PHAA. At the submarine mound locations, the interface between
 526 the series affected by and unaffected by the HIL are characterised by a sharp, strong acoustic
 527 impedance contrast (Fig. 5d). The HIL crosscuts the stratigraphic series and rise towards the seafloor
 528 at the mound locations without revealing any particular internal organisation compared to
 529 stratigraphic boundaries. At the location of complex shaped pockmarks, the interface between the
 530 series affected and unaffected by the HIL is continuous and sometimes tends to align with
 531 stratigraphic boundaries (Fig. 5e).

532 **Table 3 : Synthesis of fluid flow manifestations as observed throughout the study area compared**
 533 **to detectable oil seeps. Pockmarks inventory are deduced from the interpretation of the 12.5m**
 534 **resolution multi-beam bathymetry. Coupling the features related to oil seep sites with non-seeping**
 535 **geophysical anomalies contributes to the understanding of the seepage potential.**

Fluid flow manifestations		Total picked-out	Oil supplying sites (SAR data)	
			Active	Percentage of correlation
Submarine mounds		17	6	30 %
Complex shaped pockmarks	Cluster of heterometric pockmarks	109	53	49 %
	Irregular isolated pockmarks	175	26	15 %
Regular shaped pockmarks	Isolated conical pockmarks	890	2	< 1%
	Aligned conical pockmarks	589	0	0 %
Total picked-up		1750	87	/
Seafloor asphalt mounds	HR bathymetry (3m)	10	5	50%
	3D bathymetry (12.5m)	50	21	42 %
Seafloor geochemical	"Probable" and "Sure" categories	58	22	38 %

coring (<1500 m)	Visual asphalt inclusion	10	4	40 %
Geophysical anomalies (n°3)	From 0 to 100 ms TWT	75	30	40 %

536 5.2. Significance of thermogenic seep sites geometry

537 5.2.1. Seafloor expressions

538 Defining characteristic features of thermogenic seeps on geophysical data is crucial for the
539 understanding of petroleum system plays, to define the best seafloor coring targets and to seek and
540 inventory extreme marine ecosystems (*Jones et al., 2014*). As demonstrated by previous studies on
541 the LCB (*Andresen, 2012; Jatiault et al., 2019, Part I*), the location of seafloor thermogenic seeps is
542 controlled by the shallow deformation related to the salt tectonics. Thermogenic pockmarks locate
543 along faults associated with the underlying diapir deformation. Therefore, the location of seafloor
544 seeps, especially clusters of heterometric pockmarks is consistently influenced by the underlying salt
545 tectonics-related fault network. Both clustered and irregular pockmarks occur above fluid-related
546 seismic anomalies, such as high-amplitude vertical pipes (*Løseth et al., 2011*), shallow HIL, BSR(s), or
547 above salt. The distinction between clustered and irregular pockmarks is facilitated using the HR
548 bathymetry, while the characteristics of the subsurface are similar. The distinction between the two
549 is sometimes tricky and can be subject to data resolution issues or could mark a temporal evolution
550 that depends on seepage persistence over time. The geometrical distinction could correspond to the
551 process evolution, one being the initial stage of the other. In actively deforming areas above salt, the
552 area affected by seepage features is likely to correspond to areas undergoing active fracturing; the
553 pinpoint versus distributed character of seeps may reflect the localised versus distributed character
554 of fracturing.

555 Previous work on the LCB reported a large number of clustered pockmarks at roughly 550 metres
556 depth (*Gay et al., 2007*), i.e. along the feather edge of the BSR at the seabed. The presence of salt is
557 known to deform the temperature field above and around diapirs (*Lucazeau et al., 2004*), and may
558 affect the salinity of formation water conditions. However, the identification of BSRs above salt

559 diapirs in this area indicates that the BGHSZ remains within the sedimentary interval at salt
560 protrusion areas (Fig. 11). The strict association between submarine mounds and spiky diapirs
561 suggests that the development of mounds depends on the degree of focusing of the hydrocarbon
562 migration system. Similar shaped submarine mounds (Pingoos) were described and interpreted as
563 composed of carbonate reefs interspersed with hydrates patches in the Norwegian Sea (**Hovland and**
564 **Svensen, 2006**), but also in the Kwanza basin interpreted as imprinting the development of
565 underlying hydrates nodules (**Serié et al., 2012**).

566 Studies conducted at the salt front of the LCB led to differentiating active from inactive sites based
567 on seafloor reflectivity strength (**Wenau et al., 2014**), applying the general criterion defined by **Sager**
568 **et al. (2003)** who relate low backscatter area to dormant sites. In our study, we observed major
569 recurrent oil seeps on SAR data that are associated with a "moderate" seafloor response (Fig. 3 in
570 **Wenau et al., 2014**).

571 Authigenic carbonate precipitation is presumed to consume methane in priority (Anaerobic
572 Oxidation of Methane; e.g. **Barnes and Goldberg, 1976; Ivanov et al., 1989; Boetius et al., 2000;**
573 **Paull and Ussler, 2008; Knittel and Boetius, 2009; Boetius and Wenzhöfer, 2013**). The seafloor
574 reflectivity strength used in this study is rather similar between oil-supplying and non-oil-supplying
575 seeps (Fig. 5), even if slope artefacts may occur. Recent studies have shown that the type of
576 carbonates is different between systems dominated by oil and gas (e.g. **Hudson, 1997; Thomas et al.,**
577 **2011; Smrza et al., 2016**), which might involve a difference in precipitation rate.

578 Pockmarks associated with pore-water and biogenic methane release occur extensively in minibasins
579 in relation to local-scale features such as polygonal faults (**Andresen and Huuse, 2011; Maia et al.,**
580 **2016**) and/or tectonic faults (**Gay et al., 2006 c**). Methanogenic carbonate precipitates even in the
581 case of a "slow seep" (**Ho et al., 2012**). The absence of positive high-amplitude anomalies (**Ho et al.,**
582 **2012**) in association with conical pockmarks therefore suggests that the associated fluid is likely pore-
583 water dominated. We have observed that pockmarks located in minibasins are steeper (~15°) and

584 more conformable compared to those located above diapirs. Let us examine the factors that could
585 explain this difference. The mid Plio-Quaternary sedimentation in salt minibasins is dominated by
586 fine-grained sediments that act as an impermeable barrier to fluid migration (**Uenzelmann-Neben,**
587 **1998; Anka et al., 2013**). The sediment type could have a strong influence on pockmark geometry;
588 the recent sedimentary overburden being gently eroded across the fluid ascent path could explain
589 the conformable geometry of minibasin pockmarks. The uplift of older/coarser Miocene/Mid-
590 Pliocene sediments (**Anderson et al., 2000**), combined with salt-induced faulting and seafloor
591 hydrates/carbonates distribution might be good candidates to generate multiple seafloor fluid
592 outlets (**Jatiault et al., 2019**). In this condition, this could explain the morphological differences
593 between thermogenic seep sites above diapirs and pore-dewatering escape features in minibasin.

594 **5.2.2. Sub-seafloor expression**

595 Oil-supplying seeps correspond to small (100m diameter) sub-circular high amplitude anomalies on
596 the seafloor amplitude map (d, e and f in Fig. 5; n°3 in Fig. 8A). The presence of a BSR shows that
597 migration is focused above diapirs and that the presence of anomalies above the base of the
598 hydrates indicates that the hydrate seal is locally breached when the fluid overpressure is too high
599 (**Cathles et al., 2010**). The vertical successions of strong reflections are interpreted as fluid escape
600 pipes (Fig. 8 G; **Löseth et al., 2011; Karstens et al., 2015**) which can be related either to vertical
601 stacking of authigenic carbonate cementations or pavements (**Hovland et al., 1987; Hovland, 2002;**
602 **Pierre and Fouquet, 2007; Römer et al., 2014**), vein-filled/ hydrate-rich sediments (**Sahling et al.,**
603 **2008**) or gas-charged sediments (**Schroot et al., 2003**).

604 Outcrops of Miocene-Pliocene sediments at the seabed are privileged leakage pathways due to
605 changes in lithologic properties from fine-grained/high cap-rock efficient upper Pliocene and
606 Quaternary silts and clays to coarser, more permeable Miocene series (**Anderson et al., 2000**) and
607 appear as privileged fluid outlets.

608 The negative impedance contrast resulting in the BSR is known to primarily reflect the presence of
609 free gas beneath the base of the hydrates stability zone, rather than the increase of impedance due

610 to the presence of hydrates above (*Holbrook, 2001*). The identification of a second BSR was reported
611 in a few case studies (*Andreassen et al., 2000; Foucher et al., 2002; Popescu et al., 2006; Posewang*
612 *and Mienert, 1999; Zander et al., 2017*) with various interpretations (changes in environmental
613 conditions, paleo BSR relics, and heavier gas components). In the LCB, the observations of a second
614 cross-cutting and negative polarity reflections exclusively occur; (1) at the crest of salt diapirs and (2)
615 in the conditions of proven thermogenic fluid seepage from the identification of recurrent slicks. The
616 second BSR could be associated with heavier gas components in conditions of abundant thermogenic
617 dysmigration (*Jatiault et al., 2019, Part I*). Stacked BSR 1 and 2 would then involve distinct
618 hydrocarbon compositions between the two layers, which excludes the hypothesis of a mix of
619 hydrocarbon components from BSR1 and BSR2, and therefore suggests distinct migration pathways.
620 In that case, the 100% methane-related BSR would probably follow a lateral path along minibasin
621 stratigraphic interfaces towards the crest of the diapir. Knowing that structure II and H hydrates are
622 stable at greater depths (*Sloan, 1990*) and considering the limited extent of BSR2, the thermogenic
623 BSRs would follow more vertical advection paths along salt flanks.

624 **5.3. Relevance of multi-scale integrated evaluation of the thermogenic** 625 **seepage potential**

626 **5.3.1. Pre-existing methodology**

627 The combination of different geophysical observations provides key features to better understand
628 hydrocarbons seep systems and fluid flow phenomena (*Serié et al., 2017*). The integration of multi-
629 proxy tools is relevant for confirming source rock maturation and for studying fluid migration across
630 sedimentary series. The technique used in pre-existing methodology has its own advantages and
631 limitations that are listed and explained below:

632 - For underexplored areas, remote sensing analysis provides a first-order approach for
633 evaluating the seepage potential (*Williams and Lawrence, 2002*). The main SAR system limitations
634 are its limited spatial resolution (Table 1) and dependency on weather conditions (1.5 to 5.5 m.s^{-1} ;
635 *Jatiault et al., 2017*). On SAR images, low backscatter areas can also be look-alikes (such as algae

636 blooms, surface micro-layer; *Mityagina et al., 2007*) and the natural origin of low radiometric
637 features without a seafloor validation therefore remains questionable, even when recurrent (*Ryan et*
638 *al., 2010*). The SAR detectability thickness threshold may prevent the recognition of active oil seeps
639 when the oil flow is low.

640 - Even low-intensity oil seep sites are detectable with seabed geochemistry using
641 fluorescence analysis (*Abrams, 2005*). The recognition of asphalt inclusions in cores demonstrates
642 the thermogenic origin of fluid migrations. However, the pinpoint nature of geochemical coring
643 means that even with a dense set of cores, the technique potentially misses a large array of active
644 seep sites.

645 - The seafloor seismic amplitude provides information on lithological modifications,
646 especially above salt diapir where the outcropping Pliocene/Miocene series constitutes privileged
647 pathways for migrating fluids.

648 - The identification of a negative polarity BSR also helped us locate focused hydrocarbon fluid
649 migration above salt diapirs (*Taylor et al., 2000; Lucazeau et al., 2004; Serié et al., 2017*). In the
650 context of a shallow underlying diapir, the associated thermal anomaly creates an upward
651 displacement of the BSR that is suitable for the formation of a hydrate-related trap for hydrocarbon
652 migration. However, the survival period of a BSR following the cessation of fluid migration remains
653 under-documented, limiting the appraisal of seepage activity.

654 **5.3.2. Improvements of the methods**

655 In addition to pre-existing methodology, the following additional data analysis can help to refine the
656 fluid flow phenomena in sedimentary basin (Fig. 12). Let us examine what are the improvements
657 performed by the integration of additional data:

658 - A detailed analysis of surface slicks better constrains oil seep sites locations and address the
659 present-day seepage expelled volumes. In this study, recurrent surface slicks were successfully linked
660 with seafloor features 98% of the time. This confirms the relevance of combining the SAR system

661 with marine geophysical surface data to constrain hydrocarbon plumbing system during the
 662 exploration workflow. The occurrence rates defined as the ratio between the amount of detected
 663 slicks and SAR data coverage range from 5 to 80% (*Jatiaux et al., 2017*). Considering that the SAR
 664 system efficiency depends on weather conditions and that active seep sites are mostly intermittent,
 665 exhaustive inventory of oil seep sites relies on a high multi-temporal satellite data coverage with at
 666 least fifty overlapping SAR scenes in our study area. The amount of oil that naturally enters the
 667 marine environment is roughly split into two equal parts between natural seepage and human
 668 activity (*Prince et al., 2003*). For quantitative geological studies, it is necessary to discriminate natural
 669 seepage to unnatural oil (*Macdonald et al., 2015*). Considering average displacement values at the
 670 sea surface in the LCB of 17 cm.s^{-1} due to surface currents and winds (*Jatiaux et al., 2017*) and
 671 assuming that slicks thinner than $0.1 \mu\text{m}$ thick are not detectable (*de Beukelear et al., 2003*), the
 672 estimated minimum detectable oil flow varies between 0.76 to 9.2 l.h^{-1} depending on the spatial
 673 resolution of SAR systems (Table 4). Considering that 4380m^3 are expelled annually from one
 674 hundred seep sites (*Jatiaux et al., 2017*), the average expelled volume of a random oil seep is
 675 estimated at 5 l.h^{-1} in the study area. This demonstrates that the expelled volume is within the order
 676 of the detectability threshold. The SAR detectability thickness threshold might therefore be too high
 677 to detect the activity of a subset of potential seep sites interpreted from seismic data.

678 **Table 4 : Minimum oil output estimation depending on the spatial resolution of different SAR**
 679 **systems.**

Satellite/ Sensor	Envisat /WSM	ERS/IMP	Cosmo-SkyMed	TerraSAR – X	RADARSAT-2
Pixel Spacing (m)	75	12.5	3-15	20	25-50
Minimum volume output (l.h^{-1})	9.2	0.76	0.18 – 0.92	1.22	3.06 – 6.13

680 - The integration of current profilers (or the use of regional metocean models when the
 681 former are not available) helps constrain probable oil migration routes through the water column
 682 and quantify the probable lateral deflection (*Jatiaux et al., 2018*).

683 - The detection of asphalt mounds on HR survey confirms that oil is migrating towards the
684 seafloor and constitutes another proof of an active oil-seep sites (*Jones et al., 2014*). The presence of
685 asphalt mounds implies that hydrocarbon dysmigration is sufficiently slow for the oil to be heavily
686 degraded and stored on the seafloor (*Head et al., 2003; Larter et al., 2003; Jones et al., 2008; Larter*
687 *et al., 2006; Peters et al., 2005; Peters et al., 2007; Jones et al., 2008*). In the present case, using
688 specific seismic attributes such as curvature identified a high proportion of the mounds and may be
689 used at least for a first screening.

690 - The computation of an RMS amplitude map of shallow subsurface (first 100 ms in this
691 study) quickly pinpointing isolated sub-circular high-amplitude anomalies likely to sign the presence
692 of fluid migration, while reducing the amplitude anomaly associated with the slope inflection.
693 Vertical stacking of anomalies, if observed on cross-sections, is a strong additional indication of
694 hydrocarbon leakage. However, the technique is irrelevant for assessing the fluid type.

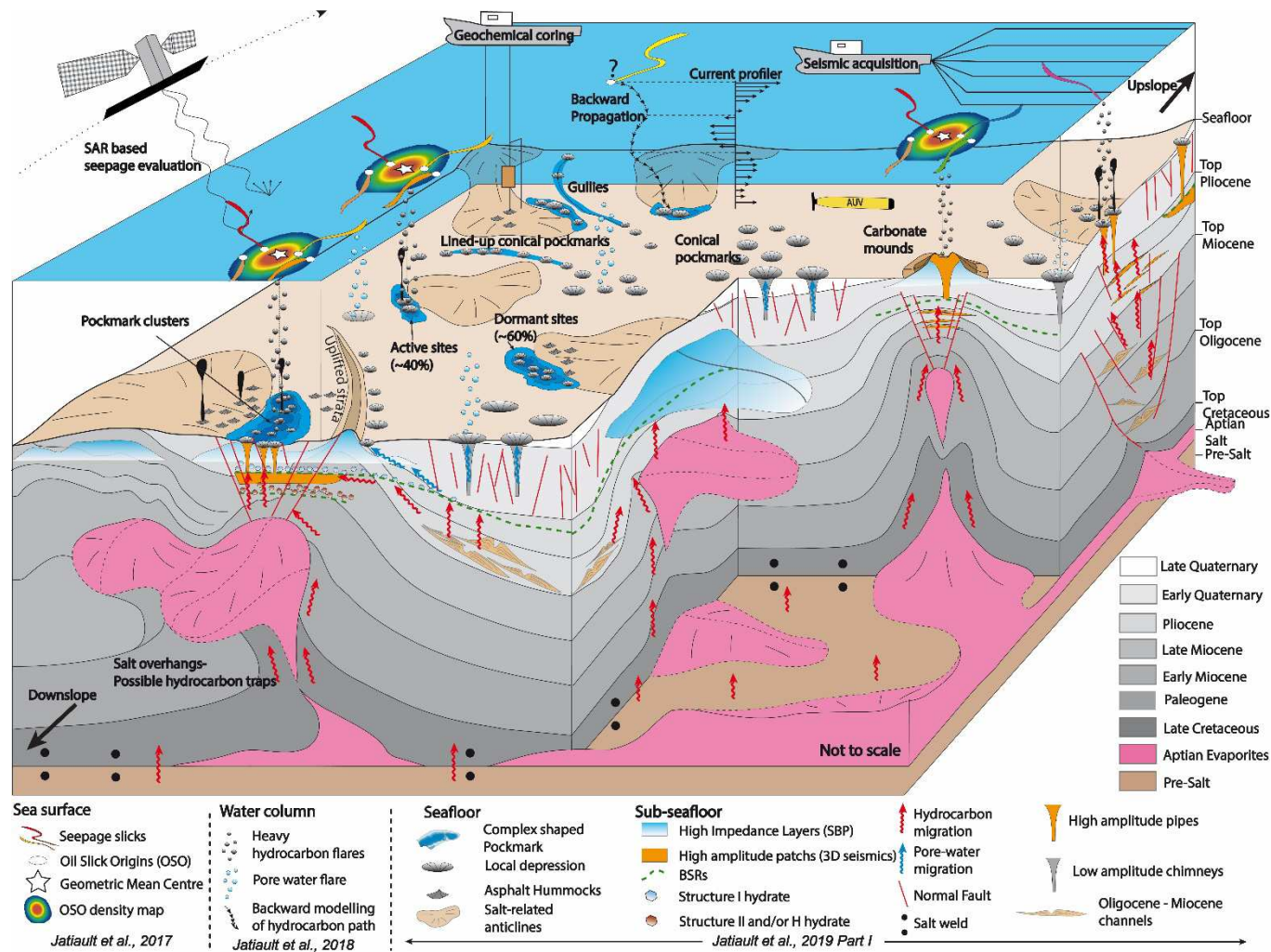
695 - We observed double BSRs only at the location of oil seeps proven by SAR analysis. Double
696 BSR could mark the basal level of stability of a mix of heavier gas. Additional studies would be
697 needed to know if this is related to compositional or concentration effects.

698 - The HIL is presumably related to limited-size carbonate slabs with shallow asphalt and
699 potentially with hydrates (*Jatiault et al., 2019, Part I*) also helps locate active hydrocarbon seepage.
700 HIL patches are typically wide, but reach the seabed in a very limited area; consequently, the
701 identification of the point where the HIL reaches the seabed reduces the uncertainty on the
702 identification of the point of seepage. The SBP dataset provide information on sub-seafloor hardness
703 and possibly a discrimination between similar shaped features, i.e. soft mud volcanoes (*Serié et al.,*
704 *2017*) compared to harder carbonate and/or hydrate mounds/pingoos (this study; *Hovland and*
705 *Svensen, 2006*). The proximity of HIL features with the seafloor also constrains seep outlets location
706 and improve the targeting of cores locations. However, the deployment of such toolsets in a given
707 area implies that the given area has already been extensively explored.

708 The combination of different observations and techniques provides an integrated vision of the
709 hydrocarbon fluid seepage phenomena in the Lower Congo Basin and helped refining the
710 methodology of studying the fluid flow phenomena (Fig. 12).

711

ACCEPTED MANUSCRIPT



712

713 Fig. 12: Synthetic block diagram illustrating the methodology and the main results concerning the characterization of the heavy hydrocarbon fluid flow in

714 the Lower Congo Basin.

715 The inventory of geophysical features associated with the oil seeps sites in this study would benefit
716 from comparative studies conducted in different geological contexts.

717 **5.4. Spatio-temporal variability of oil seepage activity**

718 The combined manifestation of recurrent sea-surface slicks and seafloor evidence of active fluid flow
719 demonstrates that liquid hydrocarbons are currently being expelled from the seafloor in the study
720 area. The combination of seismic data together with SAR imagery and geochemical features validated
721 the natural origin of the seepage (*Serié et al., 2017*). We highlighted a series of geophysical features
722 (seafloor and subsurface) associated with oil-seep systems that were extrapolated towards similar
723 fluid flow features that could also be responsible for thermogenic escapes, namely potential oil-seep
724 sites. Both geochemical and geophysical evidence demonstrate that many potential seep sites were
725 not associated with recurrent sea-surface slicks. The present-day seepage activity observed on SAR
726 data corresponds to 40 % of the total array of potential oil seep sites detected on the seafloor and
727 sub-surface (Table 3). The remaining 60 % of geophysical anomalies n°3 present the same
728 characteristics as active oil seep sites and most of them (75 %) are overlain by a seafloor fluid-flow
729 feature, which shows that most are active at seismic resolution scale and suggest much longer
730 emission frequencies.

731 The active array proportion is concordant with results published in the Gulf of Mexico, where 50% of
732 geophysical anomalies identified on seismic datasets correspond to an active oil seep site at the sea
733 surface (*Garcia-Pineda et al., 2010*). Oil seep sites are mostly transient with a widespread range of
734 periods of recurrence (*Garcia-Pineda et al., 2010; Garcia-Pineda et al., 2015; Jatiault et al., 2017*).
735 The SAR data collection dates from 1994 to 2016, which is very brief in comparison to geological time
736 scales. The remaining 60% of geophysical anomalies could also be associated with dormant seep sites
737 whose inactive stages: (1) exceed the SAR monitoring period (22 years), or (2) are shorter than SAR
738 acquisition intervals (varying from few hours to few months).

739 Barely half of seafloor areas characterised by seafloor asphalt presence (seafloor mounds and oil-
740 impregnated cores) are currently supplying oil. Using fluorescence as a proxy for oil gravity (**Abrams,**
741 **2005**), seafloor samples in our study area range from 10 to 40°API. High biodegradation leads to an
742 increase in the density of the oil in the reservoirs (**Head et al., 2003; Peters et al., 2007**) but also in
743 the shallow sub-surface (e.g. **Zengler et al., 1999; Wilkes et al., 2001**), so that biodegraded oils can
744 reach density values greater than that of ocean water (**Larter et al., 2003**). For oil when the °API
745 gravity is below that of ocean water (10), asphalts remain stored on the seafloor (**Macdonald et al.,**
746 **2004; Jones et al., 2014**). Bathymetric hummocky features, reportedly composed of a large volume
747 of stored asphalt on the seafloor, have already been observed in other provinces without sea surface
748 manifestations (**Keller et al., 2007; Valentine et al., 2010**).

749 Extreme marine ecosystems are highly reactive to hydrocarbon flow fluctuations with a survival
750 period following seepage extinction of about one year (**Hessler et al., 1988; Shanks, 1995; Shank et**
751 **al., 1998; Mullineaux et al., 2000**). In-situ records of photo/video from ROV dives would greatly help
752 ascertain the presence of modern chemosynthetic communities and therefore address the seeping
753 mechanism and activity of the remaining 60% dormant geophysical anomalies (**Charlou et al., 2004,**
754 **Gay et al., 2006a, Marcon et al., 2014**).

755 Comparable studies conducted in similar geological context, yet revealed a much tenuous oil seepage
756 manifestations (**Serié et al., 2017**). Recent sedimentation stage of the LCB were particularly high due
757 to the establishment of the Congo DSF during Neogene and upwelling system during Early
758 Quaternary (**Savoye et al., 2000; Ferry et al., 2004; Seranne and Anka, 2005; Marcano et al., 2013**),
759 which lead to salt-related deformation enhancement. The tectonic regime of seeping provinces,
760 mostly transitional in Kwanza basin and compressive in LCB could play a significant role on expelled
761 volumes.

762 6. Summary and Conclusions

763 We used several tools to assess the seepage potential in the distal salt province of the Lower
764 Congo Basin. The analysis of sea-surface oil manifestations imaged with satellite imagery,
765 coupled with a dense geochemical core-set and seafloor/ sub-seafloor manifestations of oil
766 presence provides an integrated approach of the present-day seepage efficiency.

- 767 • The geophysical features of thermogenic seeps sites previously recognised at local scale
768 (*Jatiault et al., 2019, Part I*) are validated at the full scale of the study area. Thermogenic
769 seeps sites (1) consist of complex-shaped features (clusters of irregular pockmarks and
770 seafloor mounds), (2) are associated with shallow high-impedance layers on the sub-bottom
771 profiler and (3) are underlain by BSR that (4) are underlain by consistent amplitude and (5)
772 are overlain by clusters of pipe-like features (PHAA).
- 773 • The knowledge of the fluid flow phenomena is improved from the integration of detailed
774 slicks map that provide a means to quantify seepage activity. The SBP data that provides a
775 discrimination technique between hydrocarbons and pore dewatering features and also
776 reveals the seafloor distribution of asphalt storage areas.
- 777 • About 40% of geophysical anomalies are associated with recurrent oil slicks at the sea
778 surface while the remaining 60% are most likely related to dormant seep sites whose
779 periodicity exceeds the 22-year SAR monitoring or are shorter than SAR scene acquisition
780 intervals.
- 781 • A large number of low-amplitude pipes (582) were identified in salt minibasins from the
782 12.5m seismic resolution that are linked with conical-shaped seafloor pockmarks, interpreted
783 as related to pore-water expulsion.
- 784 • Extensive high amplitudes related to the uplift of older/coarser/ more permeable sediments
785 due to the salt tectonics and characterised by extensive near-surface positive amplitude
786 geophysical anomalies appear to correspond to preferential seafloor thermogenic migration
787 outlets.

- 788 • Only 20% of BSRs are double, and these occur exclusively in association with thermogenic
789 hydrocarbons seeps.

790 **Acknowledgements**

791 The authors express their grateful thanks to Total SA, Total Angola (TEPA) and partners for the data
792 disclosure approval of the industrial seismic and sub-bottom profiler data. The authors thank Total
793 team DSO for the geochemical analysis. This work was performed in the frame of a PhD project
794 (CIFRE convention) granted by the ANRT (Agence Nationale de la Recherche et de la Technologie, No.
795 2014/0308), funded by Total SA in collaboration with University of Perpignan, France. The authors
796 thank the European Space Agency (Envisat WSM, IMP) for the delivering of free-access data. Seismic
797 interpretation was carried out using Total's proprietary software Sismage. We kindly thank
798 Christophe Serié and an additional reviewer who provided critical suggestions in order to improve
799 the impact and benefits of the paper.

800 **References**

- 801 Abrams, M.A. (2005). Significant of hydrocarbon seepage relative to petroleum generation and
802 entrapment, *Marine and Petroleum Geology* 22, p. 457-477.
- 803 Anderson, J. E., Cartwright, J., Drysdall, S. J., & Vivian, N. (2000). Controls on turbidite sand
804 deposition during gravity-driven extension of a passive margin: examples from Miocene sediments in
805 Block 4, Angola. *Marine and Petroleum Geology*, 17(10), 1165-1203.
- 806 Andreassen, K., Mienert, J., Bryn, P., & Singh, S. C. (2000). A double gas-hydrate related bottom
807 simulating reflector at the Norwegian continental margin. *Annals of the New York Academy of*
808 *Sciences*, 912(1), 126-135.
- 809 Andresen, K. J., Huuse, M., Schodt, N. H., Clausen, L. F., & Seidler, L. (2011). Hydrocarbon plumbing
810 systems of salt minibasins offshore Angola revealed by three-dimensional seismic analysis. *AAPG*
811 *bulletin*, 95(6), 1039-1065.

- 812 Andresen K.J., & Huuse, M. (2011). 'Bulls-eye' and polygonal faulting in the Lower Congo Basin:
813 Relative timing and implications for fluid expulsion during shallow burial, *Marine Geology* 279, 111-
814 127, <http://dx.doi.org/10.1016/j.margeo.2010.10.016>.
- 815 Andresen, K.J. (2012). Fluid flow features in hydrocarbon plumbing systems: What do they tell us
816 about the basin evolution, *Marine Geology*, 332-334, 89-108,
817 <http://dx.doi.org/10.1016/j.margeo.2012.07.006>.
- 818 Anka, Z., Berndt, C., Gay, A., (2012). Hydrocarbon leakage through focused fluid flow systems in
819 continental margins, *Marine Geology* p 332-334.
- 820 Anka, Z., Ondrak, R., Kowitz, A., Schodt, N. (2013). Identification and numerical modeling of
821 hydrocarbon leakage in the Lower Congo Basin: Implications on the genesis of km-wide seafloor
822 mounded structures, *Tectonophysics*, 604, 153-171, <http://dx.doi.org/10.1016/j.tecto.2012.11.020>.
- 823 Anka, Z., Séranne, M., Lopez, M., Scheck-Wenderoth, M., & Savoye, B. (2009). The long-term
824 evolution of the Congo deep-sea fan: A basin-wide view of the interaction between a giant
825 submarine fan and a mature passive margin (ZaiAngo project), *Tectonophysics* 470, 42-56,
826 <http://dx.doi.org/10.1016/j.tecto.2008.04.009>.
- 827 Barnes, R. O., & Goldberg, E.D. (1976). Methane production and consumption in anoxic marine
828 sediments. *Geology* 4:297–300.
- 829 Barwise, T., & Hay, S. (1996). Predicting oil properties from core fluorescence.
- 830 Berndt, C., Bünz, S., Clayton, T., Mienert, J., & Saunders, M. (2004). Seismic character of bottom
831 simulating reflectors: examples from the mid-Norwegian margin. *Marine and Petroleum*
832 *Geology*, 21(6), 723-733.
- 833 Boetius, A., Ravensschlag, K., Schubert, C. J., Rickert, D., Widdel, F., Gieseke, A., ... & Pfannkuche, O.
834 (2000). A marine microbial consortium apparently mediating anaerobic oxidation of methane.
835 *Nature*, 407(6804), 623-626.

- 836 Boetius, A., & Wenzhöfer, F. (2013). Seafloor oxygen consumption fuelled by methane from cold
837 seeps. *Nature Geoscience*, 6(9), 725-734.
- 838 Brice, S.E., Cochran, M.D., Pardo, G., & Edwards, A.D. (1982). Tectonics and sedimentation of the
839 South Atlantic Rift Sequence: Cabinda, Angola. *American Association Petroleum Geologists Memoir*,
840 34, 5– 18.
- 841 Brownfield, M.E., & Charpentier, R.R. (2006). Geology and total petroleum systems of the west-
842 central coastal province (7203), west Africa (No. 2207-B).
- 843 Bünz, S., Mienert, J., Bryn, P., & Berg, K. (2005), Fluid flow impact on slope failure from 3D seismic
844 data: a case study in the Storegga Slide. *Basin Research*, 17(1), 109-122.
- 845 Burwood, R., (1999). Angola: source rock control for Lower Congo Coastal and Kwanza Basin
846 petroleum systems, Geological Society, London, Special Publications v. 152, p181-184.
- 847 Carruthers, D., Cartwright, J., Jackson, M. P., Schutjens, P. (2013). Origin and timing of layer-bound
848 radial faulting around North Sea salt stocks: New insights into the evolving stress state around rising
849 diapirs. *Marine and Petroleum Geology*, 48, 130-148.
- 850 Cartwright, J., Huuse, M., & Aplin, A. (2007). Seal bypass systems. *AAPG bulletin*, 91(8), 1141-1166.
- 851 Cathles, L. M., Su, Z., & Chen, D. (2010). The physics of gas chimney and pockmark formation, with
852 implications for assessment of seafloor hazards and gas sequestration. *Marine and petroleum*
853 *Geology*, 27(1), 82-91.
- 854 Charlou, J.L., Donval, J.P., Fouquet, Y., Ondreas, H., Knoery, J., Cochonat, P., Levaché, D., Poirier, Y.,
855 Jean-Baptiste, P., Fourré, E., Chazallon, B. (2004). Physical and chemical characterization of gas
856 hydrates and associated methane plumes in the Congo–Angola Basin *Chemical Geology*, 205, 405 –
857 425, <http://dx.doi.org/10.1016/j.chemgeo.2003.12.033>.

- 858 Cole, G. A., Requejo, A.G., Ormerod, D., Yu, Z., Clifford, A. (2000). Petroleum geochemical assessment
859 of the Lower Congo Basin, in Mello, M.R., and Katz, B.J., eds., Petroleum systems of South Atlantic
860 margins: AAPG Memoir 73, p.325-339.
- 861 Cunningham, R., & Lindholm, R. M. (2000). AAPG Memoir 73, Chapter 8: Seismic Evidence for
862 Widespread Gas Hydrate Formation, Offshore West Africa.
- 863 De Beukelear, S.M., MacDonald, I.R., Guinasso, N.L., Murray, J.A. (2003). Distinct side-scan sonar,
864 RADARSAT SAR, and acoustic profiler signatures of gas and oil seeps on the Gulf of Mexico slope,
865 *Geo-Marine Letters*, 23, 177-186.
- 866 Ferry, J. N., Babonneau, N., Mulder, T., Parize, O., & Raillard, S. (2004). Morphogenesis of Congo
867 submarine canyon and valley: implications about the theories of the canyons formation.
868 *Geodinamica Acta*, 17(4), 241-251.
- 869 Fort, X., Brun, J.P., & Chauvel, F. (2004). Salt tectonics on the Angolan margin, synsedimentary
870 deformation processes, *AAPG Bulletin*, 88:11, 1523–1544.
- 871 Foucher, J. P., Nouzé, H., & Henry, P. (2002). Observation and tentative interpretation of a double
872 BSR on the Nankai slope. *Marine Geology*, 187(1), 161-175.
- 873 Gade, M., Alpers, W. (1998). Imaging of biogenic and anthropogenic ocean surface films by the
874 multifrequency/ multipolarization SIR-C/X-SAR, *Journal of Geophysical Research*, 103, 18851-18866.
- 875 Garcia-Pineda, O., MacDonald, I., Zimmer, B., Shedd, B., Roberts, H. (2010). Remote-sensing
876 evaluation of geophysical anomaly sites in the outer continental slope, northern Gulf of Mexico,
877 *Deep-Sea research II* 57, 1859-1869, <http://dx.doi.org/10.1016/j.dsr2.2010.05.005>.
- 878 Garcia-Pineda, O., MacDonald, I., Silva, M., Shedd, W., Asl, S. D., Schumaker, B. (2015).
879 Transience and persistence of natural hydrocarbon seepage in Mississippi canyon, Gulf of
880 Mexico. *Deep Sea Research Part II: Topical Studies in Oceanography*, 129, 119-129.

- 881 Gay, A., Lopez, M., Berndt, C., Séranne, M. (2007). Geological controls on focused fluid flow
882 associated with seafloor seeps in the Lower Congo Basin, *Marine Geology* 244, 68 – 92,
883 <http://dx.doi.org/10.1016/j.margeo.2007.06.003>.
- 884 Gay, A., Lopez, M., Cochonat, P., Levaché, D., Sermondadaz, G., Seranne, M. (2006 a). Evidences of
885 early to late fluid migration from an upper Miocene turbiditic channel revealed by 3D seismic coupled
886 to geochemical sampling within seafloor pockmarks, Lower Congo Basin, *Marine and Petroleum*
887 *geology* 23, 387-399, <http://dx.doi.org/10.1016/j.marpetgeo.2006.02.004>.
- 888 Gay, A., Lopez, M., Cochonat, P., Séranne, M., Levaché, D., Sermondadaz, G. (2006 b). Isolated
889 seafloor pockmarks linked to BSRs, fluid chimneys, polygonal faults and stacked Oligocene–
890 Miocene turbiditic paleochannels in the Lower Congo Basin, *Marine Geology* 226, 25 – 40,
891 <http://dx.doi.org/10.1016/j.margeo.2005.09.018>.
- 892 Gay, A., Lopez, M., Cochonat, P., Sultan, N., Cauquil, E., & Brigaud, F. (2003). Sinuous pockmark belt
893 as indicator of a shallow buried turbiditic channel on the lower slope of the Congo Basin, West
894 African Margin. In: Van Rensbergen, P., Hillis, R.R., Maltman, A.J., Morley, C.K., Subsurface Sediment
895 Mobilization, Geological Society of London, Special Publications, vol. 216, 173–189.
- 896 Gay, A., Lopez, M., Ondreas, H., Charlou, J.L., Sermondadaz, G., Cochonat, P. (2006 c). Seafloor facies
897 related to upward methane flux within a Giant Pockmark of the Lower Congo basin, *Marine Geology*
898 226, 81 – 95, <http://dx.doi.org/10.1016/j.margeo.2005.09.011>.
- 899 Guillon, S., & Keskes, N. (2004). Sismage and the 3d visualization at total. In AAPG International
900 Conference: October (pp. 24-27).
- 901 Haacke, R. R., Westbrook, G. K., & Hyndman, R. D. (2007). Gas hydrate, fluid flow and free gas:
902 Formation of the bottom-simulating reflector. *Earth and Planetary Science Letters*, 261(3), 407-420.

- 903 Haq, B. U., Hardenbol, J., & Vail, P. R. (1987). The new chronostratigraphic basis of Cenozoic and
904 Mesozoic sea level cycles. Timing and depositional history of eustatic sequences: constraints on
905 seismic stratigraphy: Cushman Foundation for Foraminiferal Research, Special Publications, 24, 7-13.
- 906 Head, I. M., Jones, D. M., Larter, S. R. (2003). Biological activity in the deep subsurface and the
907 origin of heavy oil. *Nature*, 426(6964), 344-352.
- 908 Heggland, R. (2002). Seismic evidence of vertical fluid migration through faults: applications of
909 chimney and fault detection. In *Proceedings from AAPG Hedburg Conference, Vancouver*.
- 910 Hessler, R. R., Smithey, W. M., Boudrias, M. A., Keller, C. H., Lutz, R. A., & Childress, J. J. (1988).
911 Temporal change in megafauna at the Rose Garden hydrothermal vent (Galapagos Rift; eastern
912 tropical Pacific). *Deep Sea Research Part A. Oceanographic Research Papers*, 35(10-11), 1681-1709.
- 913 Hill, A. J., Southgate, J. G., Fish, P. R., & Thomas, S. (2011). Deepwater Angola part I: Geohazard
914 mitigation. *Frontiers in Offshore Geotechnics II*, 209-214.
- 915 Ho, S., Cartwright, J.A., Imbert, P., (2012). Vertical evolution of fluid venting structures in relation to
916 gas flux, in the Neogene, Quaternary of the Lower Congo Basin, Offshore Angola.
- 917 Holbrook, W. S. (2001). Seismic studies of the Blake Ridge: Implications for hydrate distribution,
918 methane expulsion, and free gas dynamics. *Natural gas hydrates: Occurrence, distribution, and*
919 *detection*, 235-256.
- 920 Hovland, M. (2002). On the self-sealing nature of marine seeps. *Continental Shelf Research*, 22(16),
921 2387-2394.
- 922 Hovland, M., Heggland, R., De Vries, M.H., & Tjelta, T.I. (2010). Unit-pockmarks and their potential
923 significance for predicting fluid flow, *Marine and Petroleum Geology* 27, 1190 – 1199,
924 doi:10.1016/j.marpetgeo.2010.02.005.
- 925 Hovland, M., Jensen, S., & Fichler, C. (2012). Methane and minor oil macro-seep systems—their
926 complexity and environmental significance. *Marine Geology*, 332, 163-173.

- 927 Hovland, M., & Judd, A. (1988). Seabed pockmarks and seepages: impact on geology, biology, and the
928 marine environment. Graham & Trotman Ltd., London, 293 pp.
- 929 Hovland, M., Talbot, M.R., Qvale, H., Olausson, S., Assberg, L. (1987). Methane-related carbonate
930 cements in pockmarks of the North Sea, *Journal of Sedimentary Petrology*, 57:5, 881 - 892.
- 931 Hovland, M., & Svensen, H. (2006). Submarine pingoes: Indicators of shallow gas hydrates in a
932 pockmark at Nyegga, Norwegian Sea, *Marine Geology* 228, pp.15–23.
- 933 Hudson, J. D. (1977). Stable isotopes and limestone lithification. *Journal of the Geological Society*,
934 133(6), 637-660.
- 935 Hustoft, S., Dugan, B., & Mienert, J. (2009). Effects of rapid sedimentation on developing the Nyegga
936 pockmark field: Constraints from hydrological modeling and 3-D seismic data, offshore mid-Norway.
937 *Geochemistry, Geophysics, Geosystems*, 10(6).
- 938 Ivanov, M. V., Lein, A. Y., Reeburgh, M. S., Skyring, G.W. (1989). Interaction of sulphur and carbon
939 cycles in marine sediments. *Evolution of the Global Biogeochemical Sulphur Cycle*. Wiley, Chichester,
940 125-79.
- 941 Jatiault, R., Dhont, D., Loncke, L., Dubucq, D. (2017). Monitoring of natural oil seepage in the Lower
942 Congo Basin using SAR observations. *Remote Sensing of Environment*, 191, 258 - 272.
943 <http://dx.doi.org/10.1016/j.rse.2017.01.031>.
- 944 Jatiault, R., Dhont, D., Loncke, L., de Madron, X. D., Dubucq, D., Channelliere, C., & Bourrin, F. (2018).
945 Deflection of natural oil droplets through the water column in deep-water environments: The case of
946 the Lower Congo Basin. *Deep Sea Research Part I: Oceanographic Research Papers*, 136, 44-61.
- 947 Jatiault, R., Loncke, L., Dhont, D., Imbert, P., Dubucq, D. (2019). Geophysical characterisation of active
948 thermogenic oil seeps in the salt province of the lower Congo basin part I: Detailed study of one oil-
949 seeping site, *Marine and Petroleum Geology*, doi: [https:// doi.org/10.1016/j.marpetgeo.2018.11.026](https://doi.org/10.1016/j.marpetgeo.2018.11.026).

- 950 Jauer, C. D., & Budkewitsch, P. (2010). Old marine seismic and new satellite radar data: Petroleum
951 exploration of north west Labrador Sea, Canada. *Marine and Petroleum Geology*, 27(7), 1379-1394.
952 doi:10.1016/j.marpetgeo.2010.03.003.
- 953 Jones, D. M., Head, I. M., Gray, N. D., Adams, J. J., Rowan, A. K., Aitken, C. M., Oldenburg, T. (2008).
954 Crude-oil biodegradation via methanogenesis in subsurface petroleum reservoirs. *Nature*, 451(7175),
955 176-180.
- 956 Jones, D.O.B. Walls, A., Clare, M., Fiske, M.S., Weiland, R.J., O'Brien, R., Touzel, D.F. (2014). Asphalt
957 mounds and associated biota on the Angolan margin, *Deep-Sea Research I*,
958 <http://dx.doi.org/10.1016/j.dsr.2014.08.010>.
- 959 Judd, A., & Hovland, M. (2007). Seabed fluid flow: the impact on geology, biology and the marine
960 environment. Cambridge University Press.
- 961 Karstens, J., & Berndt, C. (2015). Seismic chimneys in the Southern Viking Graben—Implications for
962 palaeo fluid migration and overpressure evolution. *Earth and Planetary Science Letters*, 412, 88-100.
- 963 Keller, E. A., Duffy, M., Kennett, J. P., & Hill, T. (2007). Tectonic geomorphology and hydrocarbon
964 induced topography of the mid-channel Anticline, Santa Barbara Basin,
965 California. *Geomorphology*, 89(3), 274-286.
- 966 King, L.H., & MacLean, B. (1970). Pockmark on the Scotian Shelf, *Geological Society of America*
967 *Bulletin*, V.81, P.3141-3148.
- 968 Knittel, K., & Boetius, A. (2009). Anaerobic oxidation of methane: progress with an unknown
969 process. *Annual review of microbiology*, 63, 311-334.
- 970 Kornacki, A.S., Kendrick, J.W., Berry, J.L. (1994). Impact of oil and gas vents and slicks on petroleum
971 exploration in the deepwater Gulf of Mexico, *Geo-Marine Letters*, 14, 160-169.

- 972 Larter, S., Wilhelms, A., Head, I., Koopmans, M., Aplin, A., Di Primio, R., Telnaes, N. (2003). The
973 controls on the composition of biodegraded oils in the deep subsurface—part 1: biodegradation
974 rates in petroleum reservoirs. *Organic Geochemistry*, 34(4), 601-613.
- 975 Larter, S., Huang, H., Adams, J., Bennett, B., Jokanola, O., Oldenburg, T., Fowler, M. (2006). The
976 controls on the composition of biodegraded oils in the deep subsurface: Part II—Geological controls
977 on subsurface biodegradation fluxes and constraints on reservoir-fluid property prediction1. *AAPG*
978 *bulletin*, 90(6), 921-938.
- 979 Loncke, L., Mascle, J., Fanil Scientific Parties (2004). Mud volcanoes, gas chimneys, pockmarks and
980 mounds in the Nile deep-sea fan (Eastern Mediterranean): geophysical evidences. *Marine and*
981 *Petroleum Geology*, 21, pp 669 – 689, doi:10.1016/j.marpetgeo.2004.02.004.
- 982 Løseth, H., Gading, M., & Wensaas, L. (2009). Hydrocarbon leakage interpreted on seismic data.
983 *Marine and Petroleum Geology*, 26(7), 1304-1319.
- 984 Løseth, H., Wensaas, L., Arntsen, B., Hanken, N., Basire, C., & Graue, K. (2001). 1000 m long gas blow-
985 out pipes. In 63rd EAGE Conference & Exhibition.
- 986 Løseth, H., Wensaas, L., Arntsen, B., Hanken, N. M., Basire, C., & Graue, K. (2011). 1000 m long gas
987 blow-out pipes. *Marine and Petroleum Geology*, 28(5), 1047-1060.
- 988 Lucazeau, F., Brigaud, F., Bouroullec, J-L. (2004). High-resolution heat flow density in the lower Congo
989 basin, *Geochemistry, Geophysics, Geosystems*, 5, <http://dx.doi.org/10.1029/2003GC000644>.
- 990 MacDonald, I. R., Bohrmann, G., Escobar, E., Abegg, F., Blanchon, P., Blinova, V., ... & Heeschen, K.
991 (2004). Asphalt volcanism and chemosynthetic life in the Campeche Knolls, Gulf of Mexico. *Science*,
992 304(5673), 999-1002.
- 993 MacDonald, I.R., Garcia-Pineda, O., Beet, A., Daneshgar Asl, S., Feng, L., Graettinger, G., French-
994 McCay, D., Holmes, J., Hu, C., Huffer, F., Leifer, I., Muller-Karger, F., Solow, A., Silva, M., Swayze,

- 995 G. (2015). Natural and unnatural oil slicks in the Gulf of Mexico. *Journal of Geophysical Research:*
996 *Oceans*, 120(12), 8364-8380.
- 997 McHargue, T.R. (1990). Stratigraphic Development of Proto-South Atlantic Rifting in Cabinda, Angola
998 – A Petroliferous Lake Basin. In Katz, B.J. (Ed.) *Lacustrine Basin Exploration Case Studies and Modern*
999 *Analogs*, 50. AAPG Memoir, p.307-326.
- 1000 MacKay, M. E., Jarrard, R. D., Westbrook, G. K., & Hyndman, R. D. (1994). Origin of bottom-simulating
1001 reflectors: geophysical evidence from the Cascadia accretionary prism. *Geology*, 22(5), 459-462.
- 1002 Maia, A. R., Cartwright, J., & Andersen, E. (2016). Shallow plumbing systems inferred from spatial
1003 analysis of pockmark arrays. *Marine and Petroleum Geology*, 77, 865-881.
- 1004 Marcano, G., Anka, Z., di Primio, R., (2013). Major controlling factors on hydrocarbon generation and
1005 leakage in South Atlantic conjugate margins: A comparative study of Colorado, Orange, Campos and
1006 Lower Congo basins, *Tectonophysics* 604, p 17-190.
- 1007 Marcon, Y., Ondréas, H., Sahling, H., Bohrmann, G., & Olu, K. (2014). Fluid flow regimes and growth of
1008 a giant pockmark, *Geology*, Vol.42, Issue 1, pp.63 – 66. <http://dx.doi.org/10.1130/G34801.1>.
- 1009 Marton, G.L., Tari, G. C., Lehmann, C. T. (2000). Evolution of the Angolan Passive Margin, West Africa,
1010 With Emphasis on Post-Salt Structural Styles. *Atlantic rifts and continental margins*, 129-149.
- 1011 Mityagina, M., Lavrova, O., & Bocharova, T. (2007). Detection and discrimination of sea surface films
1012 in the coastal zone of northeastern Black Sea using SAR data. *ESA-ed*, 1.
- 1013 Moss, J. L., & Cartwright, J. (2010). 3D seismic expression of km scale fluid escape pipes from offshore
1014 Namibia. *Basin Research*, 22(4), 481-501.
- 1015 Mullineaux, L. S., Fisher, C. R., Peterson, C. H., & Schaeffer, S. W. (2000). Tubeworm succession at
1016 hydrothermal vents: use of biogenic cues to reduce habitat selection error?. *Oecologia*, 123(2), 275-
1017 284.

- 1018 Nyblade, A. A., & Robinson, S. W. (1994). The african superswell. *Geophysical research letters*, 21(9),
1019 765-768.
- 1020 O'Brien, G. W., Lawrence, G. M., Williams, A. K., Glenn, K., Barrett, A. G., Lech, M., Summons, R. E.
1021 (2005). Yampi Shelf, Browse Basin, North-West Shelf, Australia: a test-bed for constraining
1022 hydrocarbon migration and seepage rates using combinations of 2D and 3D seismic data and
1023 multiple, independent remote sensing technologies. *Marine and Petroleum Geology*, 22(4), 517-549.
1024 doi:10.1016/j.marpetgeo.2004.10.027.
- 1025 Ondreas, H., Olu, K., Fouquet, Y., Charlou, J.L., Gay, A., Dennielou, B., Donval, J.P., Fifis, A., Nadalig, T.,
1026 Cochonat, P., Cauquil, E., Bourillet, J.F., Le Moigne, M., Sibuet, M. (2005). ROV study of a giant
1027 pockmark on the Gabon continental margin, *Geo-Marine Letters*, 25, 281-292,
1028 <http://dx.doi.org/10.1007/s00367-005-0213-6>.
- 1029 Oluboyo, A.P., Gawthorpe, R.L., Bakke, K., Hadler-Jacobsen, F. (2014). Salt tectonic controls on deep-
1030 water turbidite depositional systems: Miocene, southwestern Lower Congo Basin, offshore Angola,
1031 *Basin Research* 26, 597–620, doi: 10.1111/bre.12051.
- 1032 Paull, C. K., & Ussler III, W. (2008). Re-evaluating the significance of seafloor accumulations of
1033 methane-derived carbonates: seepage or erosion indicators?.
- 1034 Peters, K. E., Walters, C. C., & Moldowan, J. M. (2005). *The biomarker guide* (Vol. 1). Cambridge
1035 University Press.
- 1036 Peters, K.E., Walters, C.C., Moldowan, J.M. (2007). *The Biomarker Guide Volume 2, Biomarkers and*
1037 *Isotopes in Petroleum Systems and Earth History*.
- 1038 Pierre, C., & Fouquet, Y. (2007). Authigenic carbonates from methane seeps of the Congo deep-sea
1039 fan. *Geo-Marine Letters*, 27(2-4), 249-257.
- 1040 Popescu, I., Lericolais, G., Panin, N., De Batist, M., & Gillet, H. (2007). Seismic expression of gas and
1041 gas hydrates across the western Black Sea. *Geo-Marine Letters*, 27(2-4), 173-183.

- 1042 Posewang, J., & Mienert, J. (1999). The enigma of double BSRs: indicators for changes in the hydrate
1043 stability field?. *Geo-Marine Letters*, 19(1-2), 157-163.
- 1044 Prince, R. C., Lessard, R. R., & Clark, J. R. (2003). Bioremediation of marine oil spills. *Oil & Gas Science
1045 and Technology*, 58(4), 463-468.
- 1046 Quirk, D. G., & Pilcher, R. S. (2012). Flip-flop salt tectonics. *Geological Society, London, Special
1047 Publications*, 363(1), 245-264.
- 1048 Riboulot, V., Sultan, N., Imbert, P., & Ker, S. (2016). Initiation of gas-hydrate pockmark in deep-water
1049 Nigeria: Geo-mechanical analysis and modelling. *Earth and Planetary Science Letters*, 434, 252-263.
- 1050 Römer, M., Sahling, H., Pape, T., dos Santos Ferreira, C., Wenzhöfer, F., Boetius, A., & Bohrmann, G.
1051 (2014). Methane fluxes and carbonate deposits at a cold seep area of the Central Nile Deep Sea Fan,
1052 Eastern Mediterranean Sea. *Marine Geology*, 347, 27-42.
1053 <http://dx.doi.org/10.1016/j.margeo.2013.10.011>.
- 1054 Ryan, J. P., Fischer, A. M., Kudela, R. M., McManus, M. A., Myers, J. S., Paduan, J. D., ... & Zhang, Y.
1055 (2010). Recurrent frontal slicks of a coastal ocean upwelling shadow. *Journal of Geophysical
1056 Research: Oceans*, 115(C12).
- 1057 Sager, W. W., MacDonald, I. R., & Hou, R. (2003). Geophysical signatures of mud mounds at
1058 hydrocarbon seeps on the Louisiana continental slope, northern Gulf of Mexico. *Marine
1059 Geology*, 198(1), 97-132.
- 1060 Sahling, H., Bohrmann, G., Spiess, V., Bialas, J., Breitzke, M., Ivaniov, I., Kasten, S., Krastel, S.,
1061 Schneider, R. (2008). Pockmarks in the Northern Congo Fan area, SW Africa: Complex seafloor
1062 features shaped by fluid flow, *Marine Geology*, 249, 206-225,
1063 <http://dx.doi.org/10.1016/j.margeo.2007.11.010>.
- 1064 Savoye, B., Cochonat, P., Apprioual, R., Bain, O., Baltzer, A., Bellec, V., ... & Crusson, A. (2000).
1065 Structure et évolution récente de l'éventail turbiditique du Zaïre: premiers résultats scientifiques des

- 1066 missions d'exploration Zaïango¹ & 2 (marge Congo–Angola). Comptes Rendus de l'Académie des
1067 Sciences-Series IIA-Earth and Planetary Science, 331(3), 211-220.
- 1068 Schoellkopf, N. B., Patterson, B.A. (2000). Petroleum systems of offshore, Cabinda, Angola, in M. R.
1069 Mello and B. J. Katz, Petroleum systems of South Atlantic margins: *AAPG Memoir 73*, 361–376.
- 1070 Schroot, B. M., & Schüttenhelm, R. T. (2003). Shallow gas and gas seepage: expressions on seismic
1071 and other acoustic data from the Netherlands North Sea. *Journal of Geochemical Exploration*, 78,
1072 305-309.
- 1073 Séranne, M., & Anka, Z. (2005). South Atlantic continental margins of Africa: a comparison of the
1074 tectonic vs climate interplay on the evolution of equatorial west Africa and SW Africa margins.
1075 *Journal of African Earth Sciences*, 43(1), 283-300.
- 1076 Séranne M., Séguret M. & Fauchier M. (1992). - Seismic super-units and post-rift evolution of the
1077 continental passive margin of southern Gabon. - *Bulletin de la Société Géologique de France*, 163, 2,
1078 135 - 146.
- 1079 Séranne M. (1999). - Early Oligocene stratigraphic turnover on the West Africa continental margin: a
1080 signature of the Tertiary greenhouse-to-icehouse transition? - *Terra Nova*, 11, 135 - 140.
- 1081 Serié, C., Huuse, M., & Schødt, N. H. (2012). Gas hydrate pingoes: Deep seafloor evidence of focused
1082 fluid flow on continental margins. *Geology*, 40(3), 207-210.
- 1083 Serié, C., Huuse, M., Schødt, N. H., Brooks, J. M., & Williams, A. (2017). Subsurface fluid flow in the
1084 deep-water Kwanza Basin, offshore Angola. *Basin Research*.
- 1085 Shanks, W. C. (1995). Mid-Ocean Ridges-Rebirth of a Sea-Floor Vent. *Nature*, 375(6526), 18-19.
- 1086 Shank, T. M., Fornari, D. J., Von Damm, K. L., Lilley, M. D., Haymon, R. M., & Lutz, R. A. (1998).
1087 Temporal and spatial patterns of biological community development at nascent deep-sea
1088 hydrothermal vents (9° 50' N, East Pacific Rise). *Deep Sea Research Part II: Topical Studies in*
1089 *Oceanography*, 45(1), 465-515.

- 1090 Shipley, T. H., Houston, H. H., & Buffler, R. T. (1979). Widespread Occurrence Of Possible Gas-Hydrate
1091 Horizons From Continental Slopes As Identified On Seismic Reflection Profiles. In Offshore
1092 Technology Conference. Offshore Technology Conference.
- 1093 Sloan, E. D. (1990). Clathrate Hydrates of Natural Gases, 1st ed., 641 pp., Marcel Dekker, New York.
- 1094 Smrzka, D., Zwicker, J., Klügel, A., Monien, P., Bach, W., Bohrmann, G., & Peckmann, J. (2016).
1095 Establishing criteria to distinguish oil-seep from methane-seep carbonates. *Geology*, 44(8), 667-670.
- 1096 Stalvies, C., Talukder, A., Ross, A., Grosjean, E., Carr, A., Williams, A.,... & Jablonski, D. (2017).
1097 Establishing hydrocarbon charge to the Ashmore Platform, Bonaparte Basin, Australia: A natural
1098 seeps study. *Marine and Petroleum Geology*, 82, 56-68.
- 1099 Taylor, M. H., Dillon, W. P., & Pecher, I. A. (2000). Trapping and migration of methane associated with
1100 the gas hydrate stability zone at the Blake Ridge Diapir: new insights from seismic data. *Marine*
1101 *Geology*, 164(1), 79-89.
- 1102 Teisserenc, P., & Villemin, J. (1989). Sedimentary basin of Gabon--geology and oil systems.
- 1103 Thomas, S., Hill, A. J., Clare, M. A., Shreeve, J. W., & Unterseh, S. (2011). Understanding Engineering
1104 Challenges Posed by Natural Hydrocarbon Infiltration and the Development of Authigenic Carbonate.
1105 In *Offshore Technology Conference*. Offshore Technology Conference.
- 1106 Thrasher, J., Fleet, A.J., Hay, S., Hovland, M. and Düppenbecker, S. (1996). Understanding geology as
1107 the key to using seepage in exploration: The spectrum of seepage styles. In: Schumacher, D. and
1108 Abrams, M.A. (eds.), *Hydrocarbon migration and its near-surface expression*. American Association
1109 of Petroleum Geologists, Memoir 66, 223-241.
- 1110 Uenzelmann-Neben, G. (1998). Neogene sedimentation history of the Congo Fan. *Marine and*
1111 *Petroleum Geology*, 15(7), 635-650.
- 1112 Unterseh, S., (2013). Early Recognition of Seabed and Sub-Seabed Natural Hydrocarbon Seeps in
1113 Deep Offshore Angola. 2013 Offshore Technology Conference, May 06 - 09, 2013, Houston, TX, USA.

- 1114 Valentine, D. L., Reddy, C. M., Farwell, C., Hill, T. M., Pizarro, O., Yoerger, D. R., ... & Clarke, B. A.
1115 (2010). Asphalt volcanoes as a potential source of methane to late Pleistocene coastal waters. *Nature*
1116 *Geoscience*, 3(5), 345-348.
- 1117 Wenau, S., Spiess, V., Pape, T., fekete, N. (2014). Cold seeps at the salt front in the Lower Congo
1118 Basin II: The impact of spatial and temporal evolution of salt-tectonics on hydrocarbon seepage,
1119 *Marine and Petroleum Geology* pp.1 – 14, <http://dx.doi.org/10.1016/j.marpetgeo.2014.09.021>
- 1120 Wilkes, H., Rabus, R., Fischer, T., Armstroff, A., Behrends, A., & Widdel, F. (2002). Anaerobic
1121 degradation of n-hexane in a denitrifying bacterium: further degradation of the initial
1122 intermediate (1-methylpentyl) succinate via C-skeleton rearrangement. *Archives of*
1123 *Microbiology*, 177(3), 235-243.
- 1124 Williams, A. & Lawrence, G. (2002). The Role of Satellite Seep Detection in exploring the South
1125 Atlantic's Ultradeep Water, in *Surface exploration case histories: Applications of geochemistry,*
1126 *magnetic, and remote sensing*, , Shumacher, D., & LeSchack, L.A., eds., *AAPG Studies in geology*
1127 *No. 48 and SEG Geophysical References Series No. 11*, 327-344.
- 1128 Zander, T., Haeckel, M., Berndt, C., Chi, W. C., Klauke, I., Bialas, J., ... & Atgin, O. (2017). On the
1129 origin of multiple BSRs in the Danube deep-sea fan, Black Sea. *Earth and Planetary Science*
1130 *Letters*, 462, 15-25.
- 1131 Zengler, K., Richnow, H. H., Rosselló-Mora, R., Michaelis, W., & Widdel, F. (1999). Methane formation
1132 from long-chain alkanes by anaerobic microorganisms. *Nature*, 401(6750), 266-269.
- 1133

Oil seep sites corresponds to complex-shaped pockmarks and carbonate mounds.

Conical pockmark located in salt-minibasins likely release pore-water.

Double bottom simulating reflectors exclusively corresponds to thermogenic seeps.

About 40% of potential oil seepage sites are currently seeping oil from the seafloor.

Additional data improved the pre-existing methodology of fluid flow studies.

ACCEPTED MANUSCRIPT